Cause and Characteristics of Changes in Mesoscale Convective Systems within a Convection-Permitting Regional Climate Model

Brendan Wallace,[a,b] Alex M. Haberlie,[a] Vittorio A. Gensini,[a] Walker S. Ashley,[a] Allison C. Michaelis, [a]

[a] *Department of Earth, Atmosphere, and Environment, Northern Illinois University, DeKalb, Illinois*

[b] *Argonne National Laboratory, Lemont, Illinois*

Corresponding author: Brendan Wallace, bwallace@niu.edu

Early Online Release: This preliminary version has been accepted for publication in *Journal of Climate*, may be fully cited, and has been assigned DOI 10.1175/JCLI-D-24-0251.1. The final typeset copyedited article will replace the EOR at the above DOI when it is published.

ABSTRACT: Changes in the frequency and intensity of mesoscale convective systems (MCS) are assessed using convection-permitting regional climate model simulations. We present a novel classification method that relates MCSs to the magnitude of their large-scale forcing environments to better understand the changing nature of MCSs across different forcing environments in a possible future climate scenario. Overall, the annual frequency, intensity, and amount of precipitation associated with MCSs are projected to increase for broad portions of the eastern conterminous United States (CONUS). Furthermore, changes in the characteristics of MCSs show larger, longer-lived, and faster MCSs particularly over the Midwest and Southeast. Seasonal examination of this response reveals a robust intensification of March–May (MAM) MCSs. The higher frequency of MAM MCSs are found to occur in weakly forced synoptic environments. Increased rainfall amounts are explained by an intensification of MCSs due to changing thermodynamics and enhanced lower-tropospheric moisture transport into the central CONUS by the North Atlantic Subtropical High. Differences in mid-latitude storm tracks are favorable towards the enhanced development of MCSs associated with strong baroclinic forcing within the Midwest and Northern Plains, but are only realized in the presence of strong changes in lower-tropospheric moisture transport. Overall, these results suggest a shift in the behavior of MAM MCSs that more closely corresponds to the behavior of June–August (JJA) MCSs in the historical climate. The increased occurrence of MCSs in weakly forced environments, particularly in MAM, deserves further investigation.

Accepted for publication in *Journal of Climate*. DOI 10.1175/JCLI-D-24-0251.1.

SIGNIFICANCE STATEMENT: Mesoscale convective systems (MCS) make large contributions to annual precipitation in the central US, but we have a limited understanding as to how they may change in a warmer climate. Using a sophisticated tracking algorithm in conjunction with output from a high resolution regional climate model, we find that MCSs will become more intense overall and occur more frequently in the Spring in the eastern US. This frequency increase is strongly supported by a greater occurrence of MCSs in environments lacking support from large-scale weather systems. Instead, simulated changes in persistent large-scale atmospheric features facilitate the climatological transport of warmer and moister air into the eastern US in Spring, supporting an enhanced MCS response.

1. Introduction

Understanding how precipitation may change in a warmer climate is of great societal importance. Globally, the mean precipitation response is constrained by the atmospheric energy budget with sensitivities ranging from 1–3% K^{-1} (Allen and Ingram 2002; Held and Soden 2006; Pendergrass 2020). Extreme precipitation, which is more dependent on low-level moisture convergence, is expected to scale closer to 7% K^{-1}, equivalent to the rate of change in the atmosphere's capacity for water vapor as dictated by the Clausius-Clapeyron equation (Trenberth et al. 2003). This rate of increase in precipitation extremes has been extensively noted in both observations (Hardwick Jones et al. 2010; Feng et al. 2016; Fischer and Knutti 2016; Taylor et al. 2017; Demaria et al. 2019) and prior modeling studies (Kharin et al. 2013; Liu et al. 2017; Prein et al. 2017a,b; Dai et al. 2020).

Within the tropics, subtropics, and midlatitudes, mesoscale convective systems (MCS) are a common source of extreme precipitation (Schumacher and Johnson 2005, 2006; Nesbitt et al. 2006). MCSs are clusters of deep convection that can organize and propagate as a singular cohesive system in environments with sufficient moisture, instability, and vertical shear (Houze 2004). These storms are hydrologically important and make substantial contributions to total annual and warm-season accumulated precipitation (Cotton et al. 1995; Haberlie and Ashley 2019b; Schumacher and Rasmussen 2020; Feng et al. 2021b). Therefore, to understand the changing nature of extreme precipitation, it is important to understand the changing nature of MCSs.

Our understanding of how MCSs will evolve in a warmer climate is largely limited by their inability to be sufficiently resolved at the horizontal grid spacings employed by most global climate

Accepted for publication in *Journal of Climate*. DOI 10.1175/JCLI-D-24-0251.1.

models (GCM) (Feng et al. 2021a). At coarser grid spacings, resolved updrafts necessary for deep convection are weaker than those simulated by models with higher resolution grids (O'Brien et al. 2016; Rauscher et al. 2016). Furthermore, the reliance on convective parameterizations has led to a prominent "drizzle bias" in most GCMs that is characterized by too frequent yet less intense precipitation than seen in observations (Gao et al. 2017; Chen et al. 2021; Wallace et al. 2023). At convection-permitting scales ($\Delta x \leq 4$ km) the overall representation of precipitation, including sub-daily extremes and diurnal timing, is vastly improved (Prein et al. 2015; Leutwyler et al. 2017; Liu et al. 2017; Ban et al. 2021; Gensini et al. 2023; Wallace et al. 2023). Consequently, the overall representation of MCSs, including their timing, size, and evolution, is also more accurate in convection-permitting models than within convection-parameterizing models (Haberlie and Ashley 2019a; Prein et al. 2020; Fitzpatrick et al. 2020; Prein et al. 2021).

Due to the high computational cost of convection-permitting simulations, a commonly used method for studying projected changes in MCSs is the pseudo-global warming technique (PGW; Schär et al. 1996; Rasmussen et al. 2011). This approach calculates a mean climate perturbation derived from a GCM ensemble and applies it to the initial fields and lateral boundaries of a regional climate model, permitting an estimate of the effects of changing thermodynamics absent substantial changes in the large-scale circulation. Using this approach, it has been found that the frequency of intense summertime MCSs may more than triple across North America and that the total MCS precipitation volume may significantly increase (Prein et al. 2017a). It has also been found that the most intense precipitation-producing regions of MCSs may disproportionately increase in size and make up a larger fraction of the overall MCS precipitation volume (Dougherty et al. 2023; Lasher-Trapp et al. 2023). Increases in the size and intensity of MCSs are consistent with changes in the thermodynamic environment, where higher precipitable water concentrations and greater values of convective available potential energy (CAPE) allow for more intense future storms (Rasmussen et al. 2020; Chen et al. 2020; Haberlie et al. 2022; Ashley et al. 2023). However, due to the limitations of the PGW approach, it is unclear how changes in the mean circulation may act to modulate the overall MCS response.

An alternative approach that is able to consider changes in both the large-scale dynamic and thermodynamic environments is to dynamically downscale output from a GCM onto a finer grid using a regional climate model (Giorgi and Gutowski 2015). Through an explicit comparison of two

Accepted for publication in *Journal of Climate*. DOI 10.1175/JCLI-D-24-0251.1.

convection-permitting regional climate models, one dynamically downscaled and one employing the PGW method, Chan et al. (2023) find that both models agreed on an overall increase in precipitation intensity and the precipitation volume attributed to MCSs. However, key characteristics of this response, including MCS size, speed, and lifetime, were sensitive to changes in vertical wind shear and, in turn, the large-scale dynamic environment. Subsequent studies analyzing the MCS response in dynamically downscaled simulations have similarly noted an overall increase in MCS activity, particularly over the eastern CONUS (Haberlie et al. 2023, 2024).

In this study, we seek to further explore the separate contributions of changes in large-scale dynamics and thermodynamics on the overall MCS response using a series of dynamically downscaled convection-permitting regional climate model simulations. Specifically, we focus on the central and eastern US, where intense MCSs account for a majority of extreme rainfall events (Schumacher and Johnson 2005, 2006), and there is relatively good agreement on an increase in the frequency and intensity of MCSs in both observational trends (Feng et al. 2016; Hu et al. 2020) and downscaled convection-permitting simulations (Haberlie et al. 2023). Through an examination of large-scale environments conducive to spring MCS initiation over the CONUS Great Plains in 20 Coupled Model Intercomparison Project Phase (CMIP) 6 models, Song et al. (2022) note an increase in the occurrence of environments characterized by a strong low-level jet and low-level southerly winds associated with an expansion of the North Atlantic Subtropical High (NASH; for more refer to Song et al. 2019). Climatologically, the NASH is characterized by a surface high centered near Bermuda (25°– 40°N, 20°– 50°W) during boreal summer (Zishka and Smith 1980). Similar results have been noted in studies examining changes in the Great Plains low-level jet in both observations (Ferguson 2022) and additional GCM ensemble studies (Zhou et al. 2021). Increased low-level jet activity is further corroborated by results based on 37 CMIP5 models that project an intensification of southerly winds along the western NASH during April–June that favors enhanced seasonal moisture transport over the eastern CONUS and results in a robust precipitation increase (Song et al. 2018a). Recent work by Haberlie et al. (2024) examined the seasonality of the MCS response within a set of dynamically downscaled convection-permitting regional climate simulations and found substantial increases in springtime MCS frequency and intensity particularly within the eastern US. However, the mechanisms underlying this response have not yet been fully disentangled and will be further examined here.

Accepted for publication in *Journal of Climate*. DOI 10.1175/JCLI-D-24-0251.1.

2. Methodology

a. Model Setup

The model data used in this study consists of a set of convection-permitting dynamically downscaled Weather Research and Forecasting (WRF) version 4.1.2 (Skamarock et al. 2019) simulations performed by Gensini et al. (2023). The model is initialized and forced at the lateral boundaries by bias-corrected output from version 1 of the Community Earth System Model (CESM; Hurrell et al. 2013) with a horizontal resolution of approximately 1°. Several 15-year periods are simulated, but for this study we only consider two: a historical simulation (HIST; 1990–2005) and an end-of-century simulation under a Representative Concentration Pathway (RCP; Moss et al. 2010) 8.5 emissions scenario (EoC85; 2085–2100). Each simulation is integrated for a full water year (1 October to 30 September) and reinitialized on 1 October for each year. These simulations are configured to have a horizontal grid spacing of 3.75 km with 51 vertical levels across a domain encompassing the CONUS (Fig. 1). Certain 2D fields such as accumulated precipitation and simulated composite reflectivity are saved at 15-minute intervals. Analysis exclusively considers the portion of the CONUS east of the Rocky Mountains (ECONUS) and consists of five sub-regions: Northern Plains, Southern Plains, Midwest, Southeast, and Northeast. Given the fine grid spacing, no deep convective parameterization is used and the impacts of shallow cumulus are simulated using the Mellor-Namada-Nakanishi-Niino dynamic multi-plume mass-flux scheme (Nakanishi and Niino 2006). For more details regarding specific model parameterizations choices, we refer the reader to Gensini et al. (2023).

To maintain the consistency of synoptic scale features between the model and the lateral boundaries, spectral nudging (Miguez-Macho et al. 2004) is used on 6-hourly intervals for select variables including three-dimensional temperature, specific humidity, zonal and meridional winds, and geopotential. Nudging is only performed above the planetary boundary layer and for scales 2,000 km or greater. Furthermore, the strength of the nudging linearly increases from the boundary layer up to the fifth level above the boundary layer. Nudging is separately applied to both the HIST and EoC85 WRF simulations and both are nudged towards their respective CESM forcing. For further details, we refer the reader to Gensini et al. (2023).

Accepted for publication in *Journal of Climate*. DOI 10.1175/JCLI-D-24-0251.1.

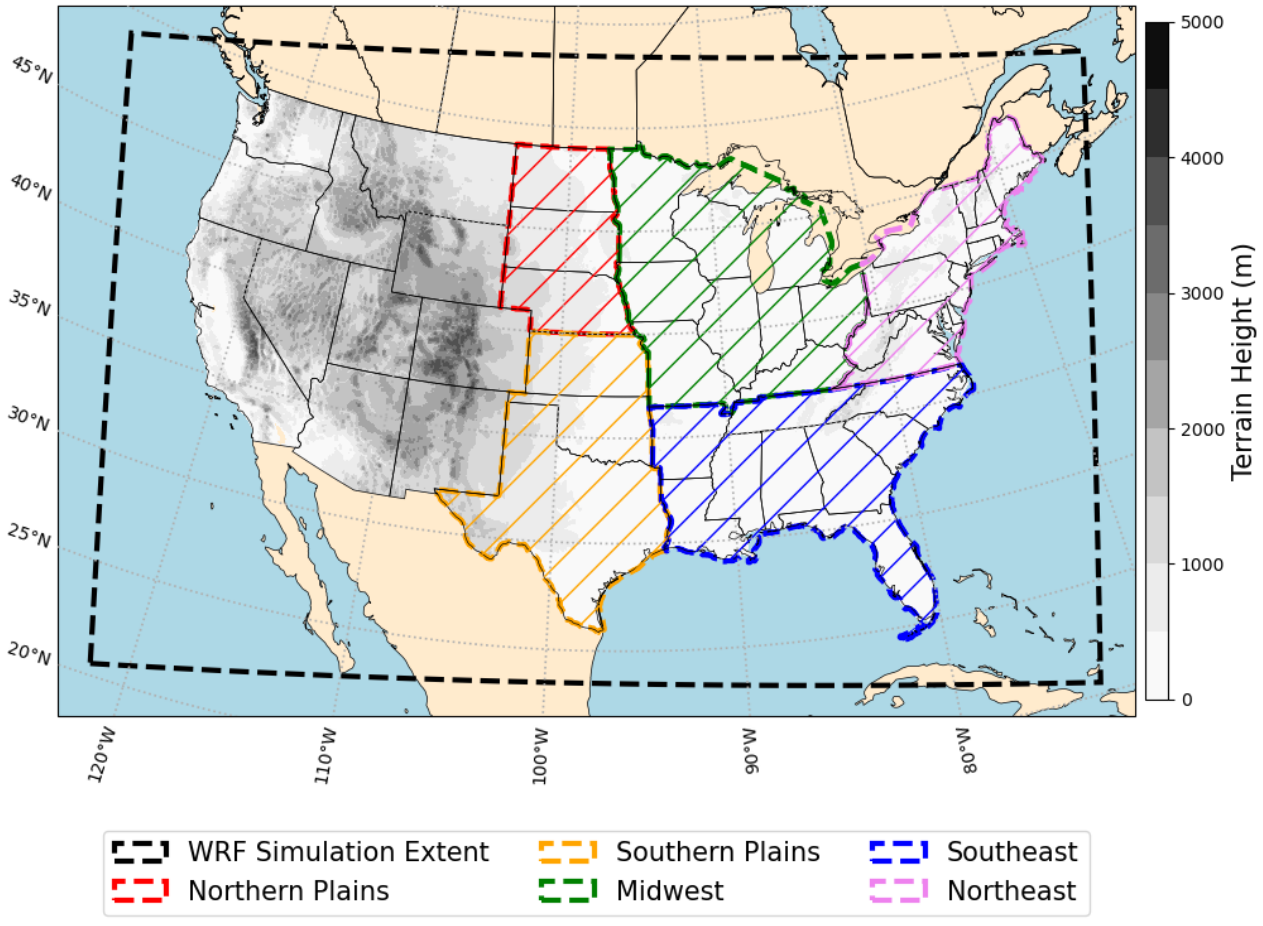

FIG. 1. Geographic extent of the WRF simulation domain and regions used to classify MCSs.

b. MCS identification and environmental classification

MCSs are identified and tracked in time based on the simulated composite (column maximum) radar reflectivity factor following the methods outlined in Haberlie and Ashley (2019b). For a comprehensive overview of the application of this methodology to this specific set of simulations, we refer the reader to Haberlie et al. (2023), but provide a brief description here. MCS features are initially identified as regions where the simulated composite reflectivity is equal to or greater than 40 dBZ with a total size of at least 40 km^2. Regions that meet the composite reflectivity criteria but not the size criteria and are within 24 km of an identified feature are merged. If the major axis length of this feature is at least 100 km, stratiform precipitation regions ($\geq$ 20 dBZ) within 96 km are combined with the feature. These features are tracked in time using spatial overlap detection. If multiple features overlap with an identified feature in the previous timestep,

Accepted for publication in *Journal of Climate*. DOI 10.1175/JCLI-D-24-0251.1.

continuity is assigned to the feature that most similarly resembles the feature in question. Finally, only MCSs that last at least 3 hours are retained for analysis. A potential limitation of this approach is that fast-moving storms or storms that experience substantial changes in morphology between timesteps may not meet the overlap criteria and would thus be misclassified as separate storms. We address this potential source of error through the use of 15-minute interval simulated composite reflectivity that minimizes the possibility of there being substantial variation in storm morphology and increases the chance that storms overlap between timesteps.

A key distinction between long-lived, intense MCSs and weaker, short-lived MCSs are their proximity to strong baroclinic forcing that often occurs in the form of a 500 hPa trough upstream of the MCS initiation location (Yang et al. 2017; Feng et al. 2019). More intense MCSs often occur in environments with a strong frontal gradient, deep moisture, and strong shear (Laing and Fritsch 2000; Coniglio et al. 2010). These conditions are not always necessary, however, as some MCSs have been shown to occur in synoptically unfavorable environments and can be attributed to eastward propagating sub-synoptic features (Pokharel et al. 2019; Song et al. 2021). Overall, changes in the magnitude and frequency of synoptic-scale features are a reflection of the large-scale dynamic response, and so it is necessary to separately consider how MCSs associated with these features may change. To do so, we classify MCSs either as strongly forced or weakly forced using a two-step categorization approach that exclusively considers 500 hPa geopotential height (Z500) (Fig. 2).

The first step considers the local finite-amplitude wave activity (LWA; Fig. 2c-d; Huang and Nakamura 2016). Prior studies have successfully used LWA derived from Z500 to examine extreme regional temperature events (Chen et al. 2015), atmospheric blocking (Martineau et al. 2017), and low-level jet coupling (Burrows et al. 2019; Ferguson 2022). The calculation of this metric is dependent on the equivalent latitude (ϕ_e), which represents the latitude where the poleward-bound area is equal to the poleward-bound area of a specific geopotential height contour (z_c). This quantity is recalculated for all geopotential height contours, and the number of contours considered is equal to the number of latitude bands within the input dataset. Regions characterized by northward or southward deviations of z_c from ϕ_e are classified as regions of anticyclonic (AWA) or cyclonic (CWA) wave activity respectively in the Northern Hemisphere. These two quantities are defined here as:

Accepted for publication in *Journal of Climate*. DOI 10.1175/JCLI-D-24-0251.1.

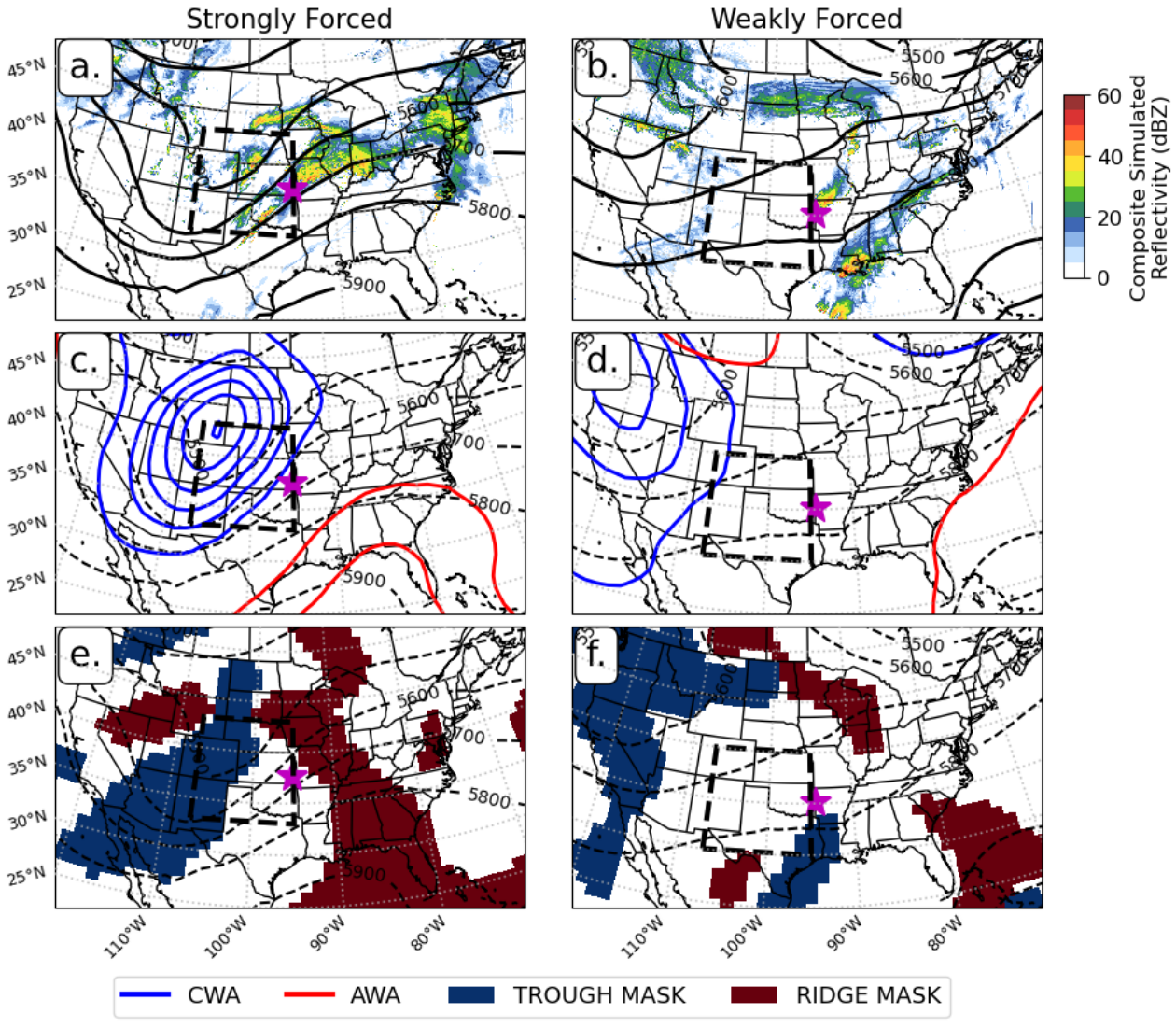

FIG. 2. Representative examples of the two types of classified MCSs at their initiation time for (a) strongly forced MCSs and (b) weakly forced MCSs along with the two derived quantities used to perform the classification. These two quantities consist of (c-d) the magnitude of CWA (blue) and AWA (red) contoured on 2 x 10^8 m^{-2} intervals and (e-f) the extent of cyclonic (blue) or anticyclonic (red) curvature based on the orientation of the 500-hPa geopotential height field. The location of the star in each panel denotes the centroid of the MCS at its initiation time. The dashed black box in each panel denotes the boundaries of the upstream box measuring 10° latitude by 12° longitude used to consider the forcing associated with the MCS.

$$AWA(\lambda,\phi_e) = \frac{a}{cos(\phi_e)} \int_{z'\geq 0,\phi\geq\phi_e(z_c)} z'(\lambda,\phi)cos(\phi)d\phi \quad (1)$$

$$CWA(\lambda,\phi_e) = -\frac{a}{cos(\phi_e)} \int_{z'\leq 0,\phi\leq\phi_e(z_c)} z'(\lambda,\phi)cos(\phi)d\phi \quad (2)$$

Accepted for publication in *Journal of Climate*. DOI 10.1175/JCLI-D-24-0251.1.

where λ is longitude, a is Earth's radius, z' is the eddy geopotential height (z' = z - z_c), and ϕ is latitude. By definition, the northward and southward deviations of z_c relative to ϕ_e are equal in area, resulting in the equal weighting of cyclones and anticyclones around the Northern Hemisphere. Furthermore, ϕ_e is re-calculated at every time-step, allowing both CWA and AWA to be unaffected by the northward shift in Z500 associated with changes in season and climate state. To consider the full extent of the Northern Hemisphere and maintain consistency with the original method, both AWA and CWA are computed every 6 hours using the Z500 field in the original bias-corrected CESM dataset used to force the WRF simulations. Following an approach similar to that of Burrows et al. (2019), an MCS is classified as strongly forced if at least half of the grid cells within a 10° latitude by 12° longitude box upstream of the MCS centroid at initiation time contain a CWA value that exceeds the 70th percentile monthly and spatially varying daily maximum. The initiation time of an MCS is the first timestep of a discrete feature that meets the criteria for classification. Furthermore, we define the MCS centroid as the unweighted central point of a classified MCS slice.

If this first criterion is not met, a secondary check is performed for upper tropospheric troughs and ridges (Fig. 2e-f) following the masking approach of Schemm et al. (2020). To be consistent with derived CWA and AWA, this quantity is also calculated every 6 hours using Z500 from the CESM dataset used to initialize and force the lateral boundaries of the downscaled WRF simulations. A gaussian smoothing filter (σ = 2) is first applied to the Z500 field to eliminate small-scale disturbances. Troughs and ridges are identified through a consideration of the curvature of Z500 (cf. Figure 2 in Schemm et al. 2020). First, the gradient of Z500 is computed for all grid cells in the Northern Hemisphere from 20° N to 90° N. Second, this gradient field is interpolated at every point to a position that is 25 km away from its original position following a vector that is rotated 90° clockwise relative to the Z500 gradient vector. Third, the 90° rotated vector relative to the Z500 gradient vector is recomputed at this new position and the angle between the original rotated vector and the displaced rotated vector is calculated. Finally, if the angle between the two vectors is greater than $\pm 0.05°$ km^{-1}, the region is identified as either a trough (positive) or ridge (negative). A check is then performed within a 10° latitude by 12° longitude box upstream of the MCS centroid at initiation time for whether 10% of the grid cells feature an identified trough or ridge feature. However, preliminary tests relying on the consideration of curvature alone performed poorly in

Accepted for publication in *Journal of Climate*. DOI 10.1175/JCLI-D-24-0251.1.

the warm season and at lower latitudes where cyclonic curvature may exist within the Z500 field absent any strong baroclinicity. To account for this, we perform an additional step that calculates the zonal and meridional average Z500 gradient from the maximum Z500 to the minimum Z500 across all latitude and longitude rows and columns respectively within the defined upstream box. If the band averaged gradient exceeds 0.01 m km^{-1} for any band and if at least 10% of points within the upstream box are identified as belonging to a trough, the MCS is classified as strongly forced. If neither criterion are met (LWA check and trough mask check), the MCS is classified as weakly forced.

3. Results

a. MCS characteristics and environments in HIST

We first consider the characteristics and large-scale environments of MCSs grouped by their forcing categorization in HIST. Consistent with Feng et al. (2019), we construct composites of large-scale environments that exclusively consider conditions at their initiation time to minimize the feedback between deep convective systems and the large-scale circulation (e.g. Chasteen and Koch 2022). An examination of the composite annual mean and anomalous Z500 for all MCSs, strongly forced MCSs, and weakly forced MCSs reveals that the classification methodology outlined in Section 2b is capable of distinguishing strongly forced MCSs from weakly forced MCSs (Fig. 3). On average, most MCSs occur in close proximity to a mid-tropospheric trough and mid-tropospheric ridge that are respectively upstream and downstream of the MCS initiation region (Fig. 3a-e). Isolating strongly forced MCSs results in an increase in the magnitude of both the time-mean and anomalous upstream trough and ridge, owing to the exclusive consideration of MCSs associated with strong baroclinic forcing (Fig. 3f-k). In contrast, MCSs associated with weak forcing environments are characterized by the absence of a pronounced mid-tropospheric trough immediately west of the initiation site and, instead, are more closely related to anomalous ridging just east of or over the region in question (Fig. 3l-p). The forcing associated with MCSs is strongly correlated to the season in which they occur (Song et al. 2019), and the results presented in Figure 3 likely reflect this. Strongly forced MCSs, that are often accompanied by a deep upper level trough, occur most often in spring (March–May; MAM) while weakly forced MCSs, that are

Accepted for publication in *Journal of Climate*. DOI 10.1175/JCLI-D-24-0251.1.

often associated with weakly zonal flow aloft, occur most often in the warm season (June–August; JJA).

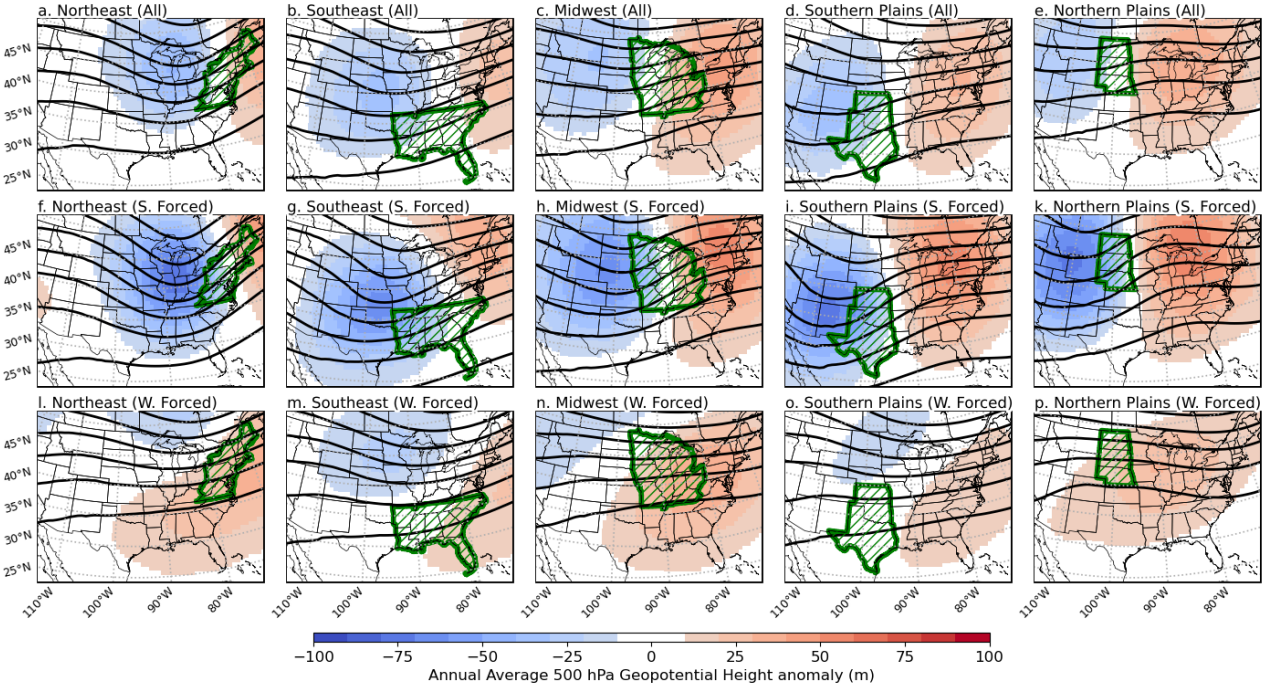

FIG. 3. Composites of annual mean 500 hPa geopotential height (contours) and anomalous 500 hPa geopotential height (shading) at the initiation time for three categories of MCSs representing: (a-e) all MCSs, (f-k) strongly forced MCSs, and (i-p) weakly forced MCSs. Columns are organized by the region containing the MCS centroid at its initiation time. The respective region is denoted by the green hatches.

We next consider the number of days annually and seasonally where at least one MCS intersects a pre-defined 75 km mesh grid. In the event that multiple MCSs occur over a particular cell within the same 0000 UTC–0000 UTC timeframe, the result is still considered as one day. Consideration of all MCSs reveals that most occur within the south-central United States annually and that the region of maximum occurrence is displaced further north towards the upper Midwest during the warmer months (Fig. 4). This MCS distribution broadly agrees with the observed MCS climatology derived from radar and satellite observations (Haberlie and Ashley 2019a; Feng et al. 2021b). Strongly forced MCSs are most common outside of JJA when comparatively less of the total seasonal MCSs are associated with strong synoptic-scale forcing (Fig. 4f-j). Instead, weakly forced MCSs make up a majority of the MCSs that occur during JJA (Fig. 4k-o). These results

Accepted for publication in *Journal of Climate*. DOI 10.1175/JCLI-D-24-0251.1.

support earlier work from Song et al. (2019) that find a reduced occurrence of strongly forced MCSs in JJA.

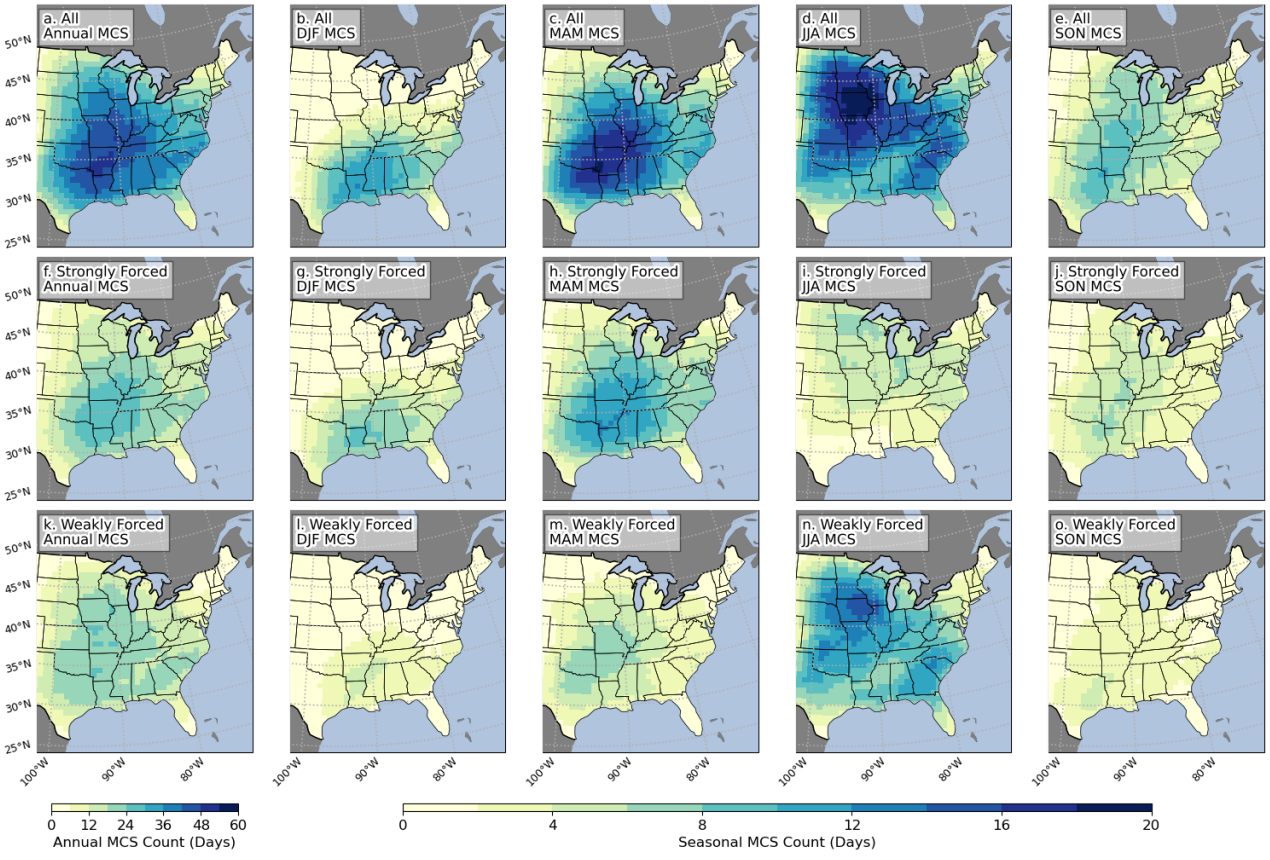

FIG. 4. Mean annual and seasonal MCS day counts for (a-e) All MCSs, (f-j) strongly forced MCSs, and (k-o) weakly forced MCSs in HIST.

The distribution of precipitation attributed to MCSs closely matches the geographic distribution of MCSs themselves (Fig. 5). The magnitude of seasonal precipitation totals is highest in DJF and MAM, particularly within the southern CONUS along the Gulf Coast (Fig. 5b,c). Despite MCSs most frequently occurring in summer, the total amount of precipitation produced by MCSs at this time is comparably smaller than what is produced earlier in the year (Fig. 5d). This can be attributed to the large occurrence of unforced MCSs at this time (Fig. 4n) that lack the large-scale support necessary to produce more precipitation across a larger area (Coniglio et al. 2010; Peters and Schumacher 2014). Consideration of the amount of accumulated precipitation attributed to strongly forced MCSs confirms this, with the highest totals occurring within the southern CONUS

Accepted for publication in *Journal of Climate*. DOI 10.1175/JCLI-D-24-0251.1.

in DJF and MAM (Fig. 5f-h). A majority of JJA precipitation is associated with weakly forced MCSs (Fig. 5n).

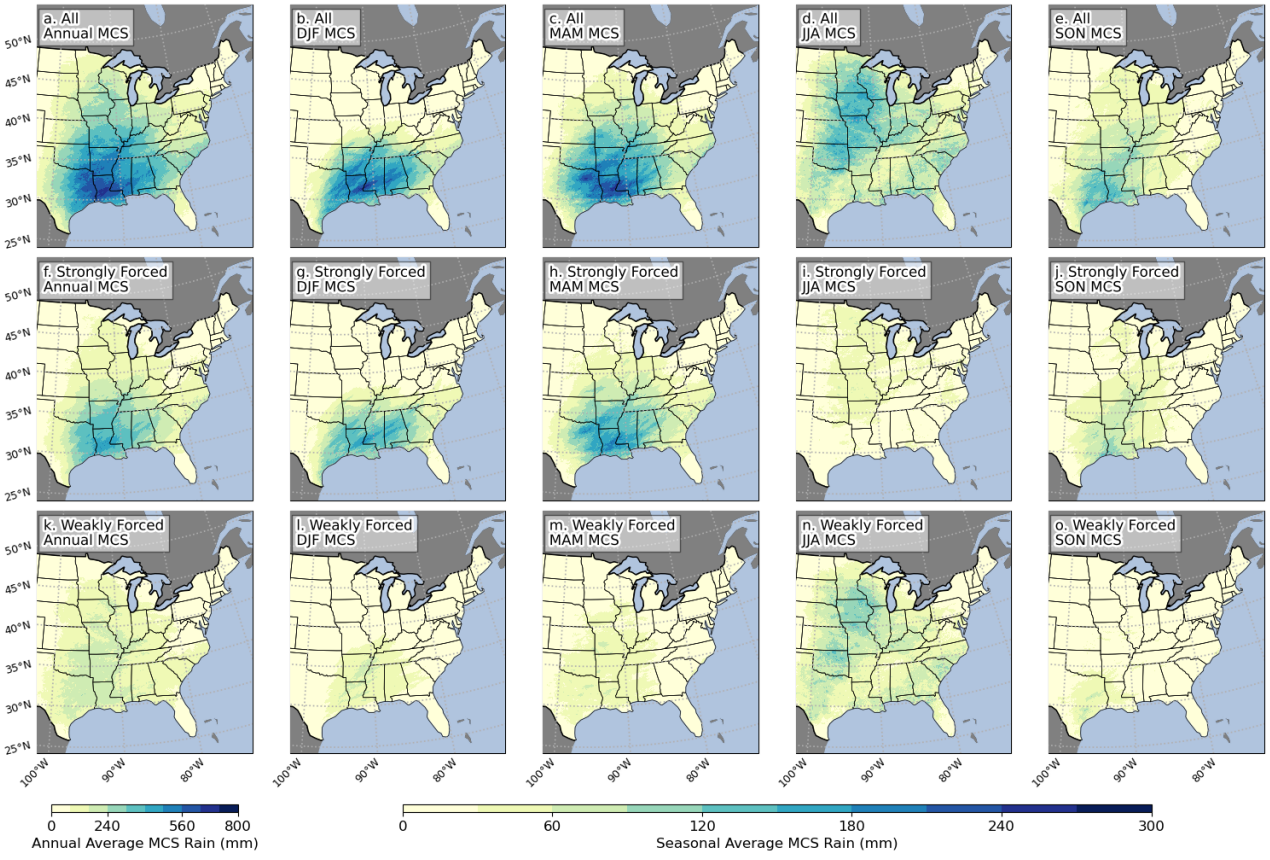

FIG. 5. Mean annual and seasonal MCS rainfall totals for (a-e) All MCSs, (f-j) strongly forced MCSs, and (k-o) weakly forced MCSs for HIST.

Results from the historical simulation are consistent with prior work examining MCS distributions within the CONUS (Haberlie and Ashley 2019a; Feng et al. 2021b; Haberlie et al. 2023) and the large-scale environments that accompany MCSs overall (Song et al. 2019; Feng et al. 2019; Na et al. 2022). While JJA appears to be the time of year where MCSs occur most often for large portions of the US east of the Rocky Mountains, the rainfall accumulations from these storms are typically smaller than those that occur in other seasons, particularly in DJF and MAM that feature the largest accumulations over the southern CONUS (Fig. 5b-c). This result agrees with earlier work from Hu et al. (2021) who note that early warm-season MCS rainfall is typically of a higher intensity and covers a larger areal extent than late warm-season MCS rainfall, and can be attributed

Accepted for publication in *Journal of Climate*. DOI 10.1175/JCLI-D-24-0251.1.

to most warm-season MCSs being weakly forced (Fig. 4n) and lacking the strong synoptic support necessary for long-lived, high accumulation storms. In the next section, we consider how MCSs in differing environments, along with the environments themselves, will change in a single realization of a future climate scenario.

b. End-of-century differences in MCS characteristics and environments

Overall, a robust increase in the number of annual MCS days is simulated across a substantial portion of the ECONUS (Fig. 6). This increase is supported by roughly equal increases in the occurrence of both strongly forced MCSs (Fig. 6f) and weakly forced MCSs (Fig. 6k). Consideration of the difference in seasonal MCS days reveals an increase in the occurrence of MAM MCSs that largely dwarfs the signal in all other seasons (Fig. 6c). Interestingly, changes in the occurrence of weakly forced MCSs (Fig. 6m) compose a larger portion of this response than changes in the occurrence of strongly forced MCSs (Fig. 6h). Also of note is a fairly consistent reduction in annual MCS days over the Southern Plains in MAM and JJA, and a broad reduction in JJA MCS days over most of the Northern Plains, portions of the Midwest, and along the western edge of the Southeast in Arkansas and Lousiana. More infrequent MCSs over the southern Plains are related to a reduced occurrence of strongly forced MCSs in MAM and weakly forced MCSs in JJA (Fig. 6h,n). The overall reduced occurrence of MCSs in JJA is more closely related to infrequent strongly forced MCSs (Fig. 6i).

Consequently, differences in the amount of accumulated rainfall from MCSs are fairly similar to the overall frequency response (Fig. 7). In the EoC85 simulations, MCSs produce more annual rainfall across most of the ECONUS (Fig. 7a) and are associated with comparatively larger contributions from the rainfall response tied to strongly forced MCSs (Fig. 7f). Despite relatively large increases in the annual occurrence of weakly forced MCSs, the changes in annual rainfall amount associated with these storms are small relative to increases in strongly forced MCS rainfall across most of the ECONUS (Fig. 7k). Separated by season, the MAM and DJF response (Fig. 7b,c) can explain a considerable share of the overall annual response (Fig. 7a). Despite stronger changes in the occurrence of weakly forced MCS, increased MAM rainfall associated with strongly forced MCSs is roughly equal to, if not greater than, increases in MAM rainfall associated with

Accepted for publication in *Journal of Climate*. DOI 10.1175/JCLI-D-24-0251.1.

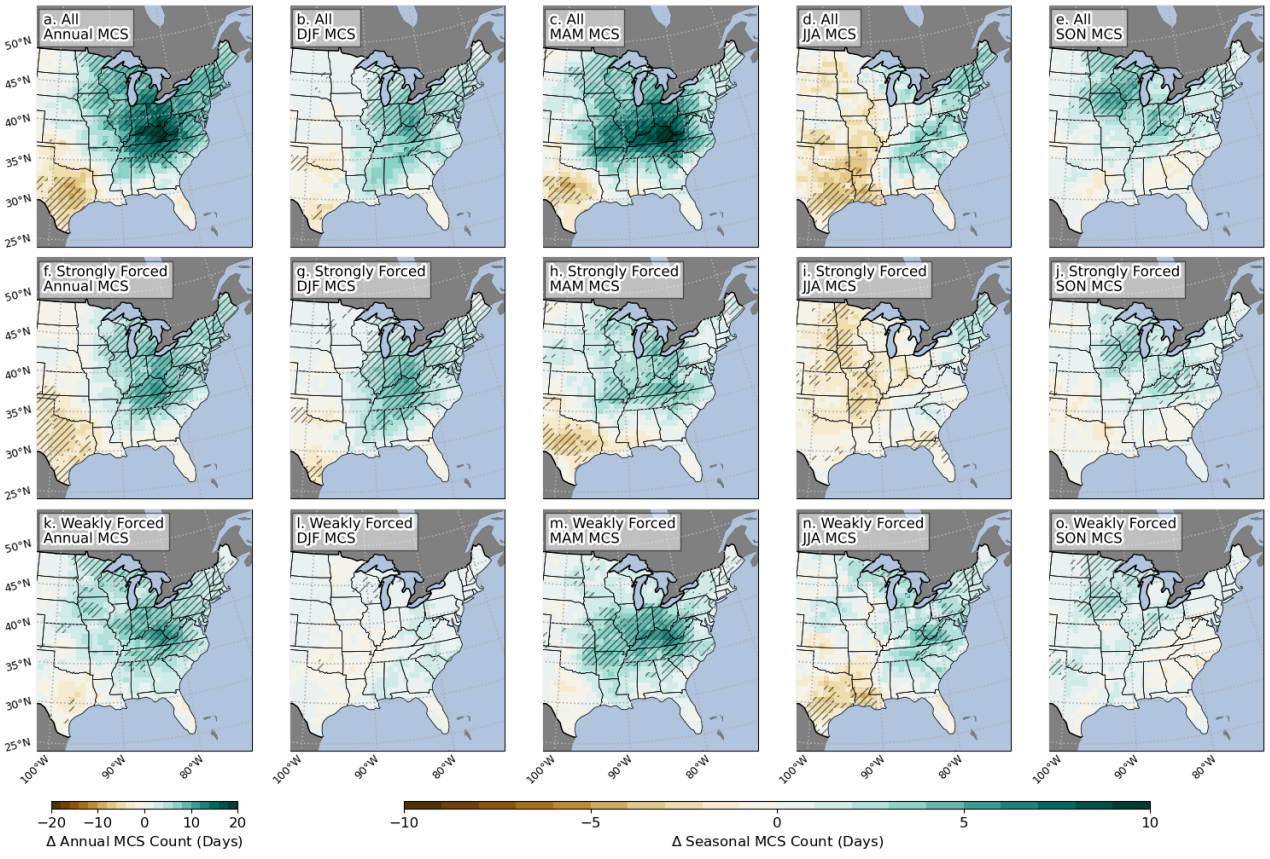

FIG. 6. EoC85–HIST differences in the mean annual and seasonal MCS day counts for (a-e) All MCSs, (f-j) strongly forced MCSs, and (k-o) weakly forced MCSs. Hatching denotes grid cells where the difference is statistically significant ($p < 0.05$) based on the Mann-Whitney U test.

weakly forced MCSs (Fig. 7h, m). Increased DJF MCS rainfall is primarily associated with greater rainfall accumulations from strongly forced MCSs (Fig. 7g).

To better understand how characteristics of MCSs are changing, we construct boxplots of annually averaged lifetime-mean total area (≥ 20 dBZ), intense area (≥ 50 dBZ), storm duration, and storm speed. We define storm speed as the distance between the storm centroid at its first and final timestep divided by the total number of timesteps the storm was active. Across both sets of simulations and for nearly all regions, strongly forced MCSs (hatched) are larger, more intense, longer-lived, and faster than weakly forced MCSs (stippled; Fig. 8). Outside of the Southern Plains and the Southeast, statistically significant increases in total storm area are simulated for almost all MCS types (Fig. 8a). Changes in the size of intense area are even more pronounced, with

Accepted for publication in *Journal of Climate*. DOI 10.1175/JCLI-D-24-0251.1.

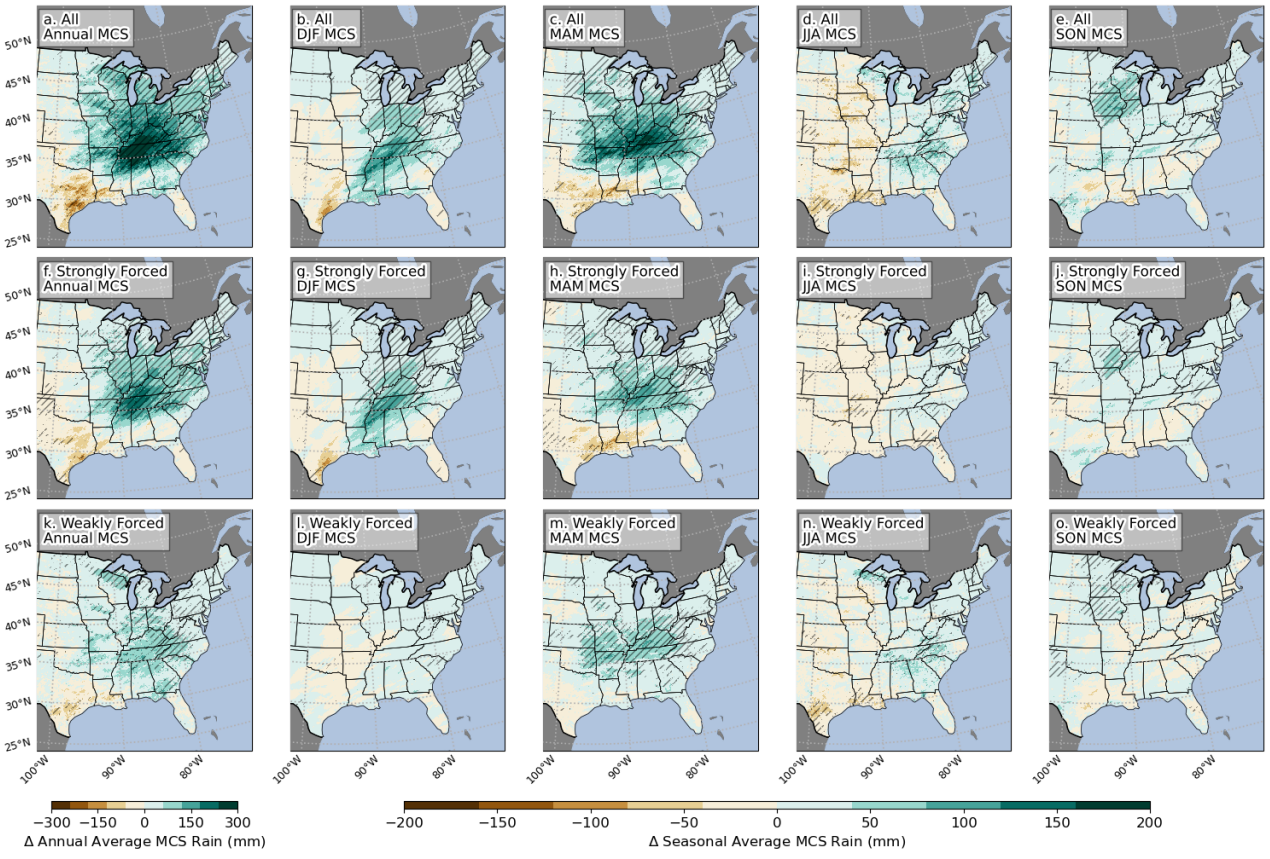

FIG. 7. EoC85–HIST differences in the mean annual and seasonal MCS rainfall totals for (a-e) All MCSs, (f-j) strongly forced MCSs, and (k-o) weakly forced MCSs. Hatching denotes grid cells where the difference is statistically significant ($p < 0.05$) based on the Mann-Whitney U test.

all MCSs in every region (except for weakly forced MCSs over the Northern Plains) experiencing statistically significant increases (Fig. 8b). These results are largely similar to earlier work from Dougherty et al. (2023) who found disproportionate increases in the most intense regions within MCSs. Over the Midwest and Northeast, two regions that see considerable overlap with areas where MCS frequency and rainfall amount are increasing (Fig. 6a; Fig. 7a), statistically significant increases in the duration of MCSs are also simulated, primarily for MCSs that occur in strongly forced environments (Fig. 8c). The lifetime mean speed of MCSs is also increasing for nearly every region except the Northern Plains, and this response is statistically significant when considering all and strongly forced MCSs within the ECONUS (Fig. 8d). Increases in the size and duration of MCSs, particularly over the Midwest and Northeast, allow for MCSs to impact a larger area in

Accepted for publication in *Journal of Climate*. DOI 10.1175/JCLI-D-24-0251.1.

the future climate and can help to explain some of the increases in MCS days simulated within those regions (Fig. 6). This is because it is easier for longer-lasting, larger MCSs to overlap over a particular region across different days. Furthermore, robust widespread increases in the areal extent of intense deep convective MCS cores ($\geq$ 50 dBZ) would support increases in MCS rain, as higher simulated reflectivity can be associated with larger rainfall rates that are able to produce more rainfall across a shorter time period (Koch et al. 2005). Larger MCSs may also help to counteract increases in the overall speed of MCSs, which, despite not being statistically significant for weakly forced MCSs and MCSs in most regions, would limit the time an MCS can produce precipitation over a particular area.

Accepted for publication in *Journal of Climate.* DOI 10.1175/JCLI-D-24-0251.1.

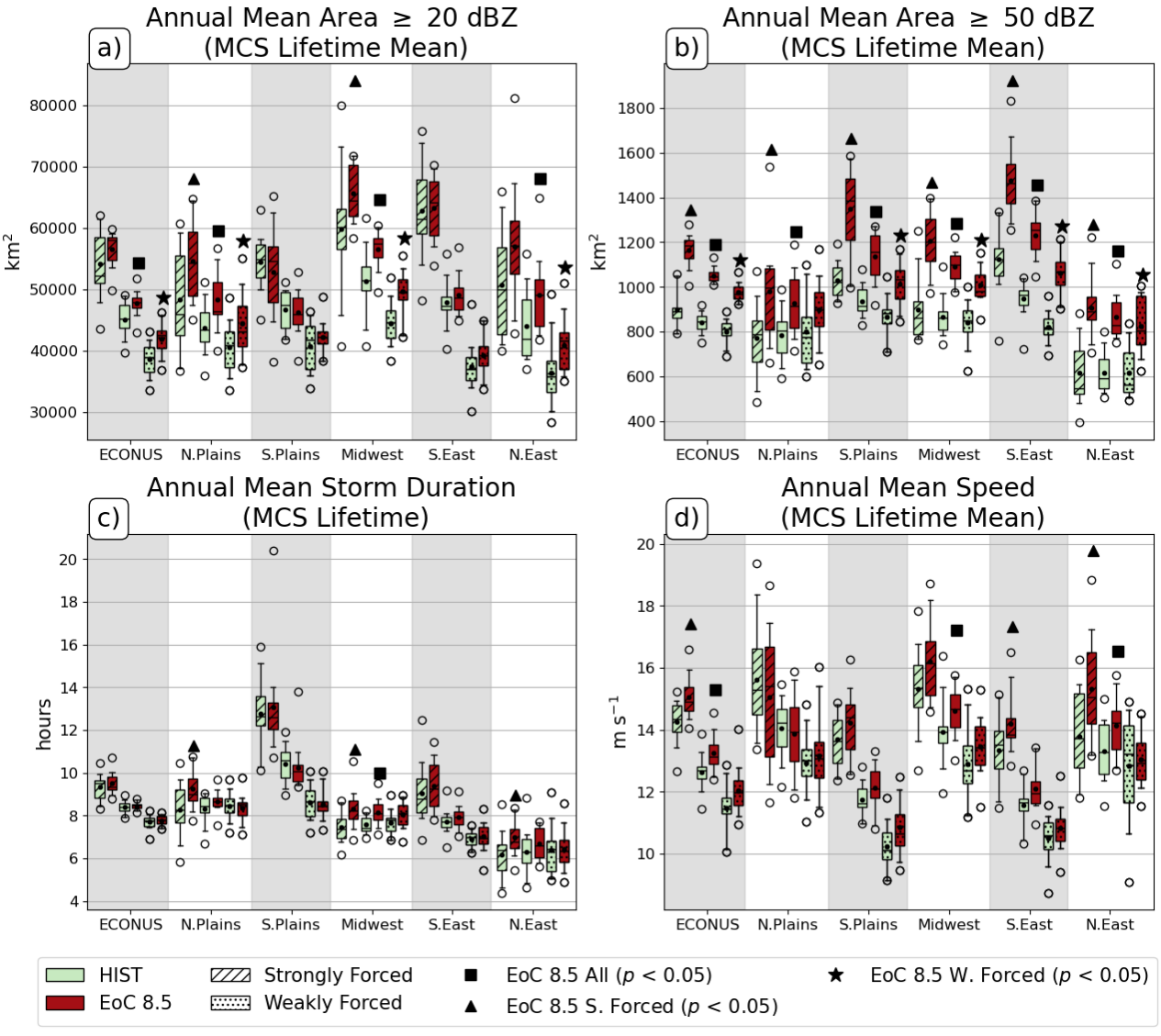

FIG. 8. Boxplots of MCS lifetime mean (a) area ≥ 20 dBz, (b) area ≥ 50 dBz, (c) duration, and (d) speed. MCSs are organized by region containing the centroid of the storm at its initiation time. An additional region representing the ECONUS is comprised of MCSs in any of the five defined regions (cf. Fig. 1). Boxes show HIST (green) and EoC85 (red) across the three MCS categories representing all MCSs (not hatched or stippled), strongly forced MCSs (hatched), and weakly forced MCSs (stippled). The box represents the interquartile range, the whiskers represent the 5th and 95th percentiles, white circles represent outliers, black dots within the box represent the mean, and the horizontal black lines represent the median. Symbols above the EoC85 box for each region and MCS category denote instances where the EoC85–HIST difference is statistically significant ($p < 0.05$) based on the Mann-Whitney U test.

Accepted for publication in *Journal of Climate*. DOI 10.1175/JCLI-D-24-0251.1.

Changes in the characteristics of MCSs indicate that they are becoming larger, faster, and longer in duration. Increases in MCS size, regardless of the strength of their associated synoptic-scale forcing, suggests changing thermodynamics as the primary driver of this response. Past studies have consistently highlighted notable increases in mean precipitable water and CAPE (Gensini and Mote 2014; Hoogewind et al. 2017; Chen et al. 2020; Rasmussen et al. 2020; Haberlie et al. 2022; Ashley et al. 2023) that support larger, more intense MCSs. Additionally, changes in the duration and speed of MCSs relate to changes in large-scale dynamics through the modification of vertical wind shear (Chan et al. 2023).

To assess the thermodynamic and dynamic environments of MCSs in both climate states, we analyze the occurrence of MCSs binned by their spatially averaged most unstable convective available potential energy (MUCAPE) and 0–6 km bulk wind shear across a 600 km^2 box centered on the MCS centroid at its initiation time (Fig. 9). Climatologically, very few MCSs occur in environments with minimal MUCAPE and shear (Fig. 9a-f). Instead, most MCSs occur in environments with moderate shear and MUCAPE with the exception of the Southeast where the maximum MCS occurrence is split between high-MUCAPE/low-shear environments and low-MUCAPE/high-shear environments. Separate consideration of the environments associated with strongly forced and weakly forced MCSs reveals that a majority of high-MUCAPE/low-shear MCSs are weakly forced while high shear low MUCAPE storms tend to be more strongly forced (not shown).

In the future climate, most regions experience the largest increase in the occurrence of MCSs that occur in high-MUCAPE/low-shear environments (Fig. 9g-m). This response would suggest a greater fraction of future MCSs occurring in weakly forced environments and is consistent with increases in the occurrence of weakly forced MCSs (Fig. 6k). A secondary maximum most prominently manifests within the Southeast and Midwest that is characterized by an increase in the occurrence of MCSs in low-MUCAPE moderate-shear environments (Fig. 9h,j). This response is consistent with annual average increases in MCS speed for these same regions (Fig. 8d) and an increased occurrence of strongly forced MCSs particularly in DJF and MAM (Fig. 6g,h). Across the Southeast and Southern, a persistent reduction in the occurrence of low MUCAPE MCSs occurs for all shear environments (Fig. 9h,m). A similar response occurs over the Midwest exclusively in low-shear environments. Using the same dataset, Haberlie et al. (2022) found that most unstable

Accepted for publication in *Journal of Climate*. DOI 10.1175/JCLI-D-24-0251.1.

convective inhibition (MUCIN) increases were maximized, primarily in JJA, within a corridor extending from south Texas northward into South Dakota. We suggest that locally maximized increases in MUCIN over these regions may disproportionately impact the occurrence of MCSs in moisture-limited regimes that lack the forcing necessary to overcome stronger inhibition.

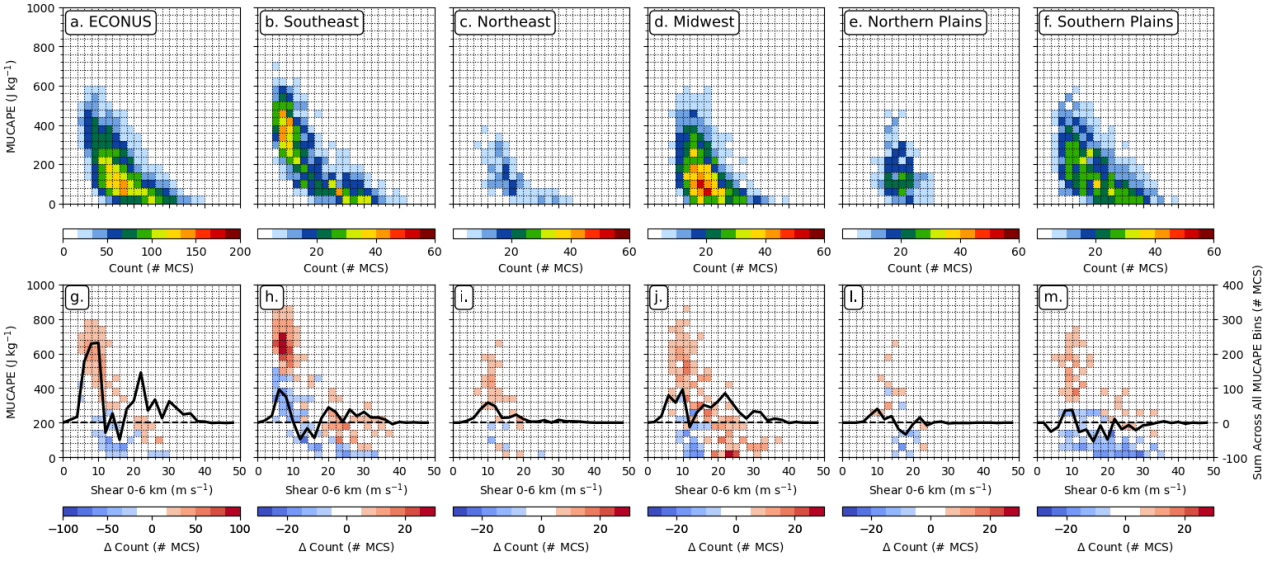

FIG. 9. 2-D histograms of MCS count binned by the magnitude of spatially averaged most unstable CAPE (MUCAPE) and 0 to 6 km bulk shear within a 600 km^2 box centered on the MCS centroid at its initiation time for (a-f) HIST and (g-m) the EoC85–HIST MCS count difference. Columns are organized by region containing the MCS centroid at initiation time. The solid line in panels g-m shows the sum across all MUCAPE bins of the MCS count difference and varies as a function of 0–6 km shear. The dashed line denotes where the sum of the difference across all MUCAPE bins is 0.

To summarize, analysis of future MCS characteristics and their environments indicate an increase in the overall frequency and intensity of MCSs. A greater occurrence of MCSs in high-MUCAPE/low-shear environments aligns well with the increased occurrence of days characterized by the passage of weakly forced MCSs (Fig. 6k). Across all regions, overall increases in the intense area of MCSs (Fig. 8b) agrees well with the increased occurrence of MCSs associated with high MUCAPE (Fig. 9g-m). Despite this, the disproportionately strong MAM MCS response in MCS frequency and total rainfall (Fig. 6c; Fig. 7c) coupled with the concentrated increase in MCS activity at the interface between the Midwest and Southeast, north of and along the Tennessee River Valley, suggests a persistent climatological feature that extends beyond increases in mean thermo-

Accepted for publication in *Journal of Climate*. DOI 10.1175/JCLI-D-24-0251.1.

dynamics alone. A study of observational MCS trends by Feng et al. (2016) finds a similar increase in the occurrence and overall intensity of April–June MCSs, with a center displaced further north and west in portions of the Midwest and Southern Plains. Through an analysis of the large-scale environment, they conclude that positive trends in geopotential height at 850 hPa concentrated in the Southeast, associated with an intensification of the western flank of the NASH, act to produce a stronger time-mean southerly wind through the central United States that enhances shear and low-level moisture transport. Similar results have also been identified by Song et al. (2018b) and Song et al. (2018a), who note general agreement amongst CMIP5 members on an intensification of the westward flank of the NASH that increases April–June precipitation in the upper Midwest and portions of the Northeast. In the next section, we limit our analysis to MAM to investigate whether a similar mechanism is responsible for the disproportionate increase in MCS occurrence and accumulated rainfall seen during this season in our set of simulations.

c. Examination of the MCS MAM response

Climatologies of geopotential height and horizontal wind on isobaric levels along with lower tropospheric (1000–700 hPa) integrated vapor transport (IVT) for MAM are overall supportive of an intensification of the NASH in EoC85 (Fig. 10). In HIST, moisture advection by low-level southerly winds directed from the Gulf of Mexico support high IVT values over the Southern Plains that curve northeast across portions of the Southeast and lower Midwest (Fig. 10a-c). Southerly wind over the central CONUS is associated with the western side of the NASH, which has been identified as a crucial mechanism that controls seasonal moisture transport and precipitation for the southeastern United States (Li et al. 2011, 2012; Nieto Ferreira and Rickenbach 2020). In the EoC85 simulations, the climatological features responsible for southerly winds and northward moisture transport intensify (Fig. 10d-f). At 900 hPa, geopotential height increases maximize along a westward extending ridge that straddles the Gulf Coast and feature an axis that aligns with the western ridge of the NASH. These height increases diminish towards the northwestern CONUS and serve to tighten a northwest–southeast aligned gradient and result in enhanced south-southeasterly flow in the central and southern US. Similar responses are observed at 850 hPa and 700 hPa and strengthen the lower-tropopsheric IVT . This intensified seasonal moisture transport into the southern Midwest region and northern Southeast region aligns well with locations that see

Accepted for publication in *Journal of Climate*. DOI 10.1175/JCLI-D-24-0251.1.

an increase in the frequency of MCSs (Fig. 6c) and the amount of rainfall produced by MCSs in MAM (Fig. 7c). Song et al. (2018a) found, using CMIP5, Spring increases in rainfall further north that could be explained by a stronger southerly component of the 925 hPa wind. This suggests that the location of the greatest positive rainfall response may demonstrate a strong sensitivity to changes in climatological moisture transport associated with the NASH.

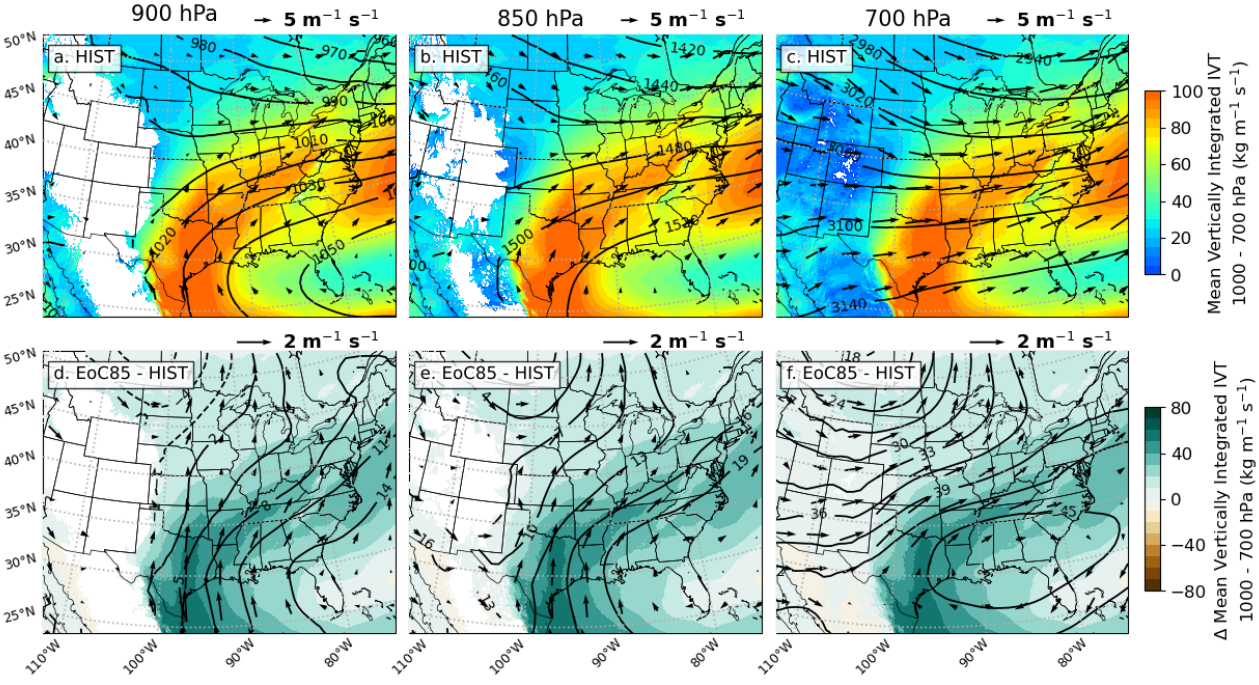

FIG. 10. MAM mean plots of geopotential height (contour), horizontal wind (vector), and 1000–700 hPa IVT (shading) at 900 hPa (left), 850 hPa (center), and 700 hPa (right) for (a-c) HIST and (d-f) the EoC85–HIST difference.

We have established a linkage between an intensification of the westward flank of the NASH and increased MCS rainfall in the eastern CONUS in a future climate that mechanistically agrees with past observational and modeling studies. However, portions of the Southern Plains and Southeast along the Gulf of Mexico receive enhanced lower-tropospheric moisture transport but demonstrate no significant increases in MCS activity (Fig. 6c). This suggests that moisture advection alone may not be enough to induce the positive precipitation response. To better understand the effect of changes in mean dynamics and thermodynamics on the overall response, we perform a decomposition of the atmospheric water budget (Seager et al. 2010; Zhang et al. 2019; Wallace and Minder 2024). For a comprehensive derivation, we refer the reader to Seager et al.

Accepted for publication in *Journal of Climate*. DOI 10.1175/JCLI-D-24-0251.1.

(2010). Through this decomposition, differences in the balance of precipitation and evaporation (δ(P–E)) can be related to differences in the strength of the climatological mean moisture flux convergence (MFC). The mean MFC difference can be decomposed into components that represent the contributions from changes in thermodynamics (TH), mean circulation (C), and transient eddies (TE) such that:

$$
\begin{aligned}
g\delta(P-E) &\approx \delta MFC_{TH} + \delta MFC_{C} + \delta MFC_{TE} - \delta S, \\
MFC_{TH} &= -\int_0^{p_s} \nabla \cdot (\overline{\vec{v}}_{HIST}[\delta\overline{q}])dp, \\
MFC_{C} &= -\int_0^{p_s} \nabla \cdot ([\delta\overline{\vec{v}}]\overline{q}_{HIST})dp, \\
MFC_{TE} &= -\int_0^{p_s} \nabla \cdot \delta(\overline{\vec{v}'q'})dp
\end{aligned} \tag{3}
$$

where overbars denote climatological means, primes denote departures from the climatological mean, δ denotes the EoC85–HIST difference, g is gravitational acceleration, p_s is surface pressure, q is specific humidity, $\vec{v}$ is horizontal wind, and p is pressure. We neglect the calculation of $\delta S = \delta(\overline{q_s\vec{v}_s \cdot \nabla p_s})$ which represents changes at the surface and has been shown to be small relative to the other terms (Seager et al. 2010; Zhang et al. 2019; Fu et al. 2021). To reduce computational expense, this analysis is performed on output from the WRF simulations that have been coarsened to have a horizontal grid spacing of 75 km.

Overall reductions in the magnitude of MFC (Fig. 11a) for portions of the Southern Plains and along the Gulf Coast, in addition to increases in the magnitude of MFC for portions of the lower Midwest extending from southern Missouri through West Virginia, align fairly well with changes in MCS rainfall (Fig. 7). These results align even more closely with the differences in total (MCS and non-MCS) MAM rainfall within these same simulations (Haberlie et al. 2023, their supplementary Figure 3). The spatial pattern of MFC_{TH} reveals that changes in specific humidity act to support reductions in the overall strength of MFC within the Southern Plains while making minimal contributions to the positive increases over the Tennessee River Valley (Fig. 11b). Since specific humidity is increasing at every grid point within the domain at every vertical level (not shown), the negative contributions of MFC_{TH} physically indicate that there is greater moisture within regions that experience divergence by the mean flow or that the gradient of humidity is changed such that it

Accepted for publication in *Journal of Climate*. DOI 10.1175/JCLI-D-24-0251.1.

increases advection by the historical climatological flow. In contrast, the contribution of MFC_C acts to increase MFC for a broad portion of the ECONUS (Fig. 11c). Physically, this indicates that the horizontal wind is changing in a manner that increases convergence given the pre-existing gradient of specific humidity. This dynamic response is consistent with changes in the magnitude of winds at 900 hPa and 850 hPa (Fig. 10d,e) which show increases in southerly wind that maximize along the Gulf Coast and steadily reduce further north. Lastly, the contribution of MFC_{TE} shows that the effect of changes in storm tracks on the overall MFC is negative across most of the ECONUS (Fig. 11d). Transient eddies, that arise from discontinuities in the mean flow, make large contributions to the total poleward moisture and energy transport in the mid-latitudes (Trenberth and Stepaniak 2003). Negative contributions of MFC_{TE} may be physically related to a strengthening of individual storms, and, in turn, enhanced poleward moisture transport to higher latitudes outside our domain (Wu et al. 2011). This suggests that changes in the strength of horizontal wind more consistently act to enhance MFC for most of the ECONUS, and physically links changes in winds, rather than changes in specific humidity, to the positive rainfall response centered over the Tennessee River Valley.

In order to explore how the climatological frequency and magnitude of individual storm tracks are changing, we consider the MAM average Z500 alongside the frequency and magnitude of CWA that exceeds 1 x 10^7 m^{-2}. The choice of this threshold for CWA is arbitrarily decided through consideration of the historical climatology of CWA and additional tests incrementally lowering the threshold to 1 x 10^6 m^{-2} did not significantly change the result. Changes in the seasonal climatology of CWA and Z500 suggest a reduced occurrence of storm tracks in the ECONUS (Fig. 12b). In HIST, moderate CWA is shown to occur over the Northeastern and Southwestern US, corresponding to the climatological position of mid-tropospheric troughs (Fig. 12a,d). This pattern is disrupted within the EoC85 simulations which feature more frequent CWA over the northwestern CONUS and a reduced occurrence and strength of CWA primarily over the eastern and southwestern CONUS (Fig. 12b,d). Differences in Z500 reveal a local minimum in height increases over the northwestern CONUS that contrasts with a local maximum over northern Mexico. This pattern of higher height increases extends towards the northeast and aligns well with the reduced frequency and magnitude of CWA within the ECONUS. There is considerable uncertainty in the robustness of this response due to the large interannual variability of CWA.

Accepted for publication in *Journal of Climate*. DOI 10.1175/JCLI-D-24-0251.1.

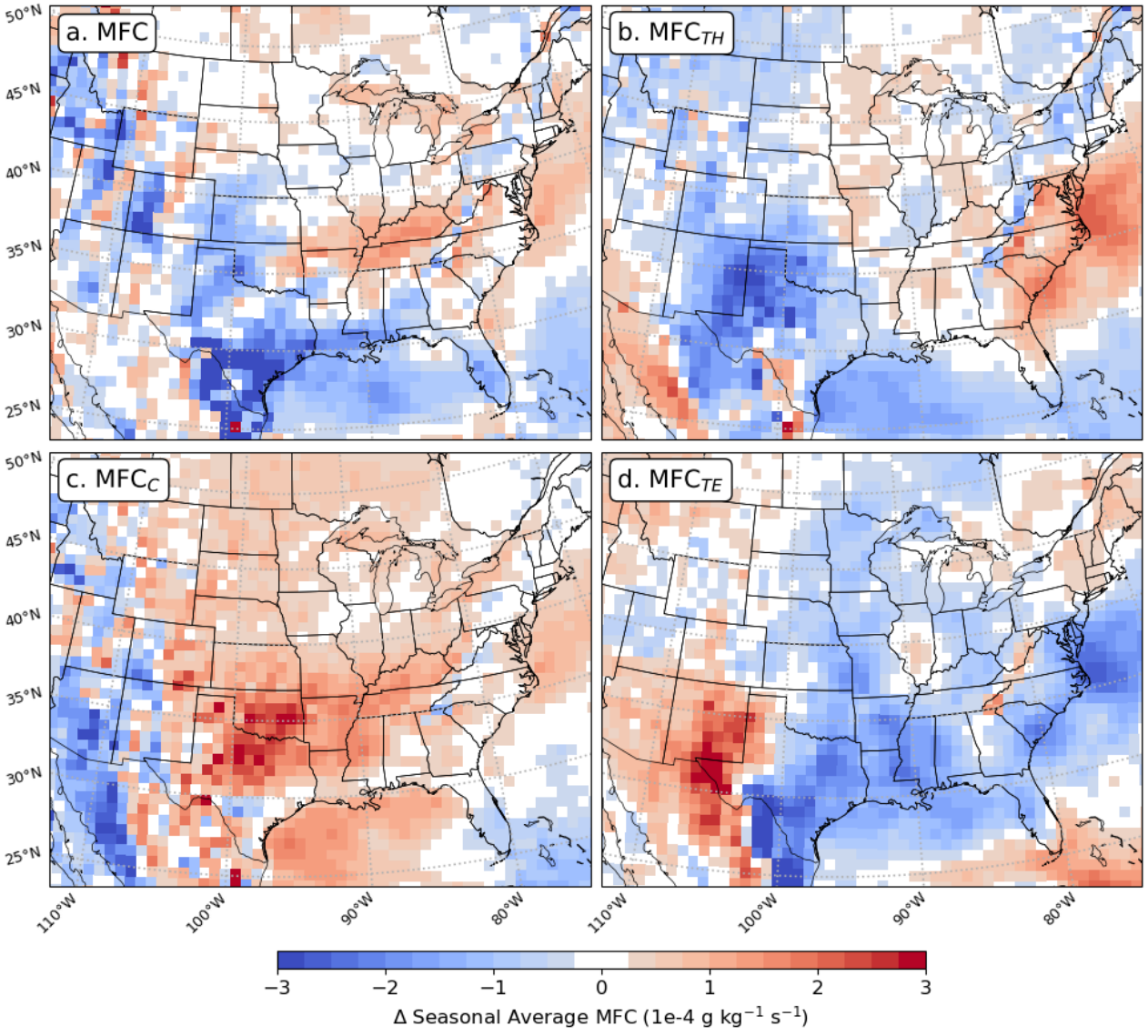

FIG. 11. EoC85–HIST MAM averaged difference in (a) MFC, (b) MFC$_{TH}$, (c) MFC$_{C}$, and (d) MFC$_{TE}$ following the decomposition outlined in Equation 3. Fields are derived from the native WRF output regridded onto a 75 km grid.

Statistically significant changes in the frequency and magnitude of CWA predominantly exist along the southern edge of the domain and are likely a spurious result due to the lower sample size of synoptic disturbances at lower latitudes (Fig. 12a). Despite this, the gradient of changes in mean geopotential height correspond well with changes in strongly forced MCSs (Fig. 6h), specifically over the Midwest and Southeast that favor an anomalous mid-tropospheric trough with an axis that

Accepted for publication in *Journal of Climate*. DOI 10.1175/JCLI-D-24-0251.1.

extends northward through the Great Plains (Fig. 3g,h). Furthermore, the reduced occurrence of CWA along the southern edge of the domain, coupled with local maxima in height increases over the same region, would suggest a reduced occurrence of storm tracks that can extend down into lower latitudes and is consistent with less strongly forced MCSs in the Southern Plains in EoC85 (Fig. 6h) and the negative contributions of transient eddies to MFC (Fig. 11d). While this change in CWA dynamically favors an enhanced occurrence of MAM MCSs over the Northern Plains, the lack of concentrated increases in lower-tropospheric moisture transport to this region (Fig. 10d-f) may help to explain the muted MCS frequency and rainfall response here (Figs. 7c, 6c).

4. Discussion

The results presented in this study help offer additional insight into characteristics of the overall MCS response to a changing climate. While the annual occurrence of MCSs (Fig. 6a) and the total annual rainfall attributed to MCSs (Fig. 7a) both increase across the ECONUS, a large portion of this increase can be attributed to changes in MAM MCSs (Fig. 6c; Fig. 7c). Separate consideration of MCSs that occur in environments characterized by strong and weak upstream baroclinic forcing reveals that, despite occurring much less often in MAM within the historical climate, an increased occurrence of weakly forced MCSs make up a large share of the MAM MCS frequency response in the future simulations (Fig. 6m). Despite this, the contributions to the difference in total MAM rainfall produced weakly and strongly forced MCSs are comparable (Fig. 7h, m). This result can be explained by the tendency for weakly forced MCSs to have shorter lifetimes and cover a smaller areal extent than strongly forced MCSs (Fig. 8). In addition, we conclude that more intense MCSs are a result of enhanced thermodynamics due to greater MUCAPE (Fig. 9; see also Haberlie et al. 2022, their Figure 4), seasonal moisture transport (Fig. 10), and convergence (Fig. 11). An overall increase in MCS intensity is supportive of earlier studies examining the MCS response to climate warming in convection-permitting models (Prein et al. 2017b; Haberlie et al. 2023; Dougherty et al. 2023).

Increases in the simulated occurrence of weakly forced MAM MCSs are consistent with an earlier onset of the warm-season (JJA) MCS regime (Fig. 4n), where limited baroclinic forcing coupled with relatively higher instability the formation of smaller, more transient storms. Through an analysis of four years of radar observations, Ferreira and Rickenbach (2021) conclude that the

Accepted for publication in *Journal of Climate*. DOI 10.1175/JCLI-D-24-0251.1.

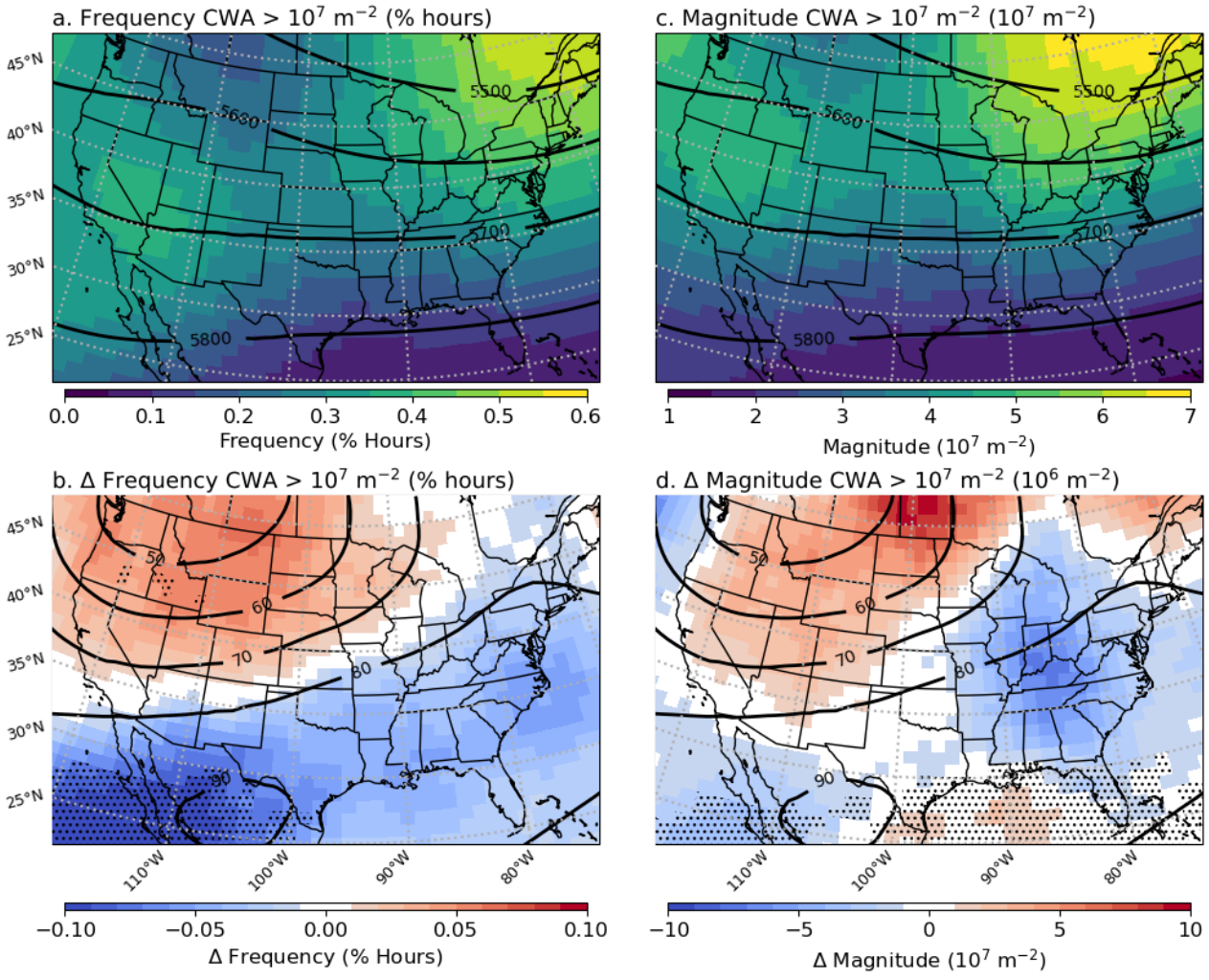

FIG. 12. Plots of the average MAM frequency of CWA and magnitude of CWA exceeding 1e7 m^{-2} (shading) and Z500 (contours) for (a, c) HIST and (b, d) the EoC85–HIST difference. Stippling is used to denote regions where the CWA frequency and magnitude difference are statistically significant ($p \leq 0.05$) based on the Mann-Whitney U test.

onset of the warm-season precipitation regime is characterized by a westward extension of the NASH coupled with poleward transport of CAPE from the Gulf of Mexico. We propose that the enhanced westward expansion of the NASH and associated low-level southerly moisture transport in MAM (Fig. 10) may act to induce a similar response in this set of simulations for spring MCSs.

There remains considerable uncertainty in how mean large-scale dynamics may change in a future climate (Pfahl et al. 2017). Because of this, we must stress that, due to computational restraints,

Accepted for publication in *Journal of Climate*. DOI 10.1175/JCLI-D-24-0251.1.

our consideration of a single downscaled GCM does not allow us to definitively state how MCSs may change for the CONUS. Furthermore, choice of model configuration, including whether or not nudging is employed and how it is implemented, may result in substantial drift between a regional climate model and its parent GCM, leading to a potentially altered depiction of how large-scale circulations may change. However, general agreement between our results and the results of past observational and modeling studies lends more credibility to the mechanisms underlying the full response. The initiation and organization of southeastern CONUS precipitation has been shown to demonstrate a sensitivity to the placement of the NASH (Li et al. 2012; Nieto Ferreira and Rickenbach 2020). Furthermore, observational trends (Li et al. 2011) and GCM ensembles (Song et al. 2018b,a) agree on an intensification of the NASH in response to warming. Our findings, that suggest a disproportionate response of springtime MCSs, also agree well with observational trends of MCSs that have occurred in the CONUS (Feng et al. 2016) and align well with expected changes in the climatological setup of the NASH. While the location of maximum precipitation changes do not exactly align with those of previous studies, this can likely be attributed to differences in the strength and positioning of the NASH in the models chosen for analysis between these varying studies. The poleward shift in storm tracks is also a well-established result within the literature and has been found in both reanalysis data (McCabe et al. 2001; Fritzen et al. 2021) and GCM ensemble projections (Yin 2005; Chang et al. 2012). Altogether, these results suggest an overall increase in the mean intensity of MCSs (Fig. 8) due to changing thermodynamics, consistent with prior studies utilizing the PGW approach (Prein et al. 2017a; Dougherty et al. 2023), and that regional variations can exist due to changes in the climatology of storm tracks and the synoptic-scale mean circulation.

5. Conclusions

We have presented results examining the MCS response to climate change in a set of dynamically downscaled WRF simulations forced by bias-corrected CESM. These simulations are performed at 3.75-km grid spacing with precipitation output saved at 15-minute intervals, allowing for a unique examination of MCSs in a warmer climate state. Two 15-year simulations are compared representing a historical (HIST; 1990–2005) and an end-of-21st-century (EoC85; 2085–2100) period under an RCP8.5 emissions scenario. Our results yield the following key findings.

Accepted for publication in *Journal of Climate*. DOI 10.1175/JCLI-D-24-0251.1.

1. In the sampled future climate state, the annual occurrence of MCSs and the total amount of rainfall attributed to MCSs increases for portions of the ECONUS and are comprised primarily of changes in MCSs that occur in MAM. Much of the total change in the frequency of MCSs is accounted for by increases in MCSs that occur in synoptically weak environments. Despite this, increases in total rainfall is composed of similar contributions from strongly forced and weakly forced MCSs.

2. Statistically significant increases in the overall size and duration of MCSs, particularly over the Southeast and Midwest, permit them to impact a larger area. Significant increases in the size of intense deep convective cores ($\geq$ 50 dBZ) indicate an overall increase in the intensity of MCSs regardless of region.

3. Within EoC85, a greater share of all MCSs occur in environments with high values of MUCAPE and low values of 0–6 km bulk shear, with the strongest regional responses occurring over the Southeast and Midwest.

4. Enhanced seasonal moisture transport, associated with an intensification of the western flank of the NASH, aids MCS development across portions of the southern Midwest and Southeast. An MFC decomposition reveals that the enhanced convergence of this moisture is primarily associated with changes in winds while changes in the spatial pattern of specific humidity along with the location and behavior of synoptic-scale storms are associated with net divergence over the Southern Plains and portions of the Southeast along the Gulf of Mexico.

5. Changes in 500 hPa height are statistically insignificant, yet suggest a westward and northward displacement of the climatological occurrence of mid-tropospheric troughs that may favor MCS development for portions of the Midwest and Southeast and disfavor MCS development over the Southern Plains. This shift dynamically supports an enhanced MCS occurrence over the Northern Plains as well, but we propose that this response is not realized due to the lack of strong changes in seasonal moisture transport to this region.

Our results suggest a shift will occur in springtime MCS behavior that more closely corresponds to behavior found within the warm-season in the historical climate. We speculate that this shift can be attributed to an intensification of the western flank of the NASH that bolsters seasonal moisture transport, permitting greater MUCAPE (see Haberlie et al. 2022, Figure 4f) and MFC that both act

Accepted for publication in *Journal of Climate*. DOI 10.1175/JCLI-D-24-0251.1.

to intensify MCSs associated with strong synoptic-scale forcing and provide additional instability to facilitate the formation of MCSs associated with weaker, sub-synoptic scale features. An increased occurrence of weakly forced MCSs suggests a reduced predictability of intense storms in a future climate (Jankov and Gallus 2004). Furthermore, MCSs that are increasingly associated with local or sub-synoptic scale forcing may further limit the effectiveness of GCMs at capturing changes in extreme precipitation due to their coarse grid spacing.

Due to the scope of this work, we are unable to fully examine other aspects of this response such as changes in the strength and magnitude of cold pools and the possible influence of enhanced springtime MCSs on land-atmosphere interactions (e.g. Hu et al. 2021). The results presented here would benefit from more dynamically-downscaled GCM studies that look for a similar MCS response in convection-permitting simulations. Due to computational limitations, future work should more closely attempt to relate MCSs to the climatological occurrence of synoptic-scale features and inter-annual modes of variability such as the El-Niño Southern Oscillation. More work examining the large-scale environments associated with MCSs (e.g. Song et al. 2022) may also be critical in better understanding results from GCMs that are capable of quantifying the uncertainty in the large-scale response but are poorly equipped to simulate MCSs. Additional research should also consider the feedback of more intense convection, due to changing thermodynamics, on the large-scale circulation (Chasteen and Koch 2022).

Accepted for publication in *Journal of Climate*. DOI 10.1175/JCLI-D-24-0251.1.

Acknowledgments. The authors would like to thank three anonymous reviewers for their comments that helped to improve the overall quality of the manuscript. The authors would also like to acknowledge high-performance computing support from Cheyenne (https://doi.org/10.5065/D6RX99HX) provided by NCAR's Computational and Information Systems Laboratory, sponsored by the National Science Foundation. This research was supported by the National Science Foundation award numbers 1637225, 1800582, and 2203516. The authors also would like to acknowledge and thank Dr. Michael Papka (NIU/Argonne) and the Argonne Leadership Computing Facility at Argonne National Laboratory for data storage and post processing assistance. The authors would also like to thank Dr. Sebastian Schemm and Dr. Michael Sprenger for providing code that helped with setting up the ridge and trough identification algorithm. This research used resources of the Argonne Leadership Computing Facility, which is a DOE Office of Science User Facility supported under Contract DE-AC02-06CH11357.

Data availability statement. The seasonal and annual average fields along with the associated analyses used to generate the figures presented in this manuscript are archived through Zenodo (Wallace 2024) and provided on Github (https://github.com/bc-wallace/mcs_paper_2024). Bias-corrected CESM used for some of the analysis and to initialize and force the lateral boundaries of the WRF simulations are available at the National Center for Atmospheric Research's Research Data Archive (Monaghan et al. 2014).

References

Allen, M. R., and W. J. Ingram, 2002: Constraints on future changes in climate and the hydrologic cycle. *Nature*, **419 (6903)**, 224–232, https://doi.org/10.1038/nature01092, URL https://www.nature.com/articles/nature01092.

Ashley, W. S., A. M. Haberlie, and V. A. Gensini, 2023: The Future of Supercells in the United States. *Bulletin of the American Meteorological Society*, **104 (1)**, E1–E21, https://doi.org/10.1175/BAMS-D-22-0027.1, URL https://journals.ametsoc.org/view/journals/bams/104/1/BAMS-D-22-0027.1.xml.

Ban, N., and Coauthors, 2021: The first multi-model ensemble of regional climate simulations at kilometer-scale resolution, part I: evaluation of precipitation. *Climate Dynamics*, **57 (1-**

Accepted for publication in *Journal of Climate*. DOI 10.1175/JCLI-D-24-0251.1.

2), 275–302, https://doi.org/10.1007/s00382-021-05708-w, URL https://link.springer.com/10.1007/s00382-021-05708-w.

Burrows, D. A., C. R. Ferguson, M. A. Campbell, G. Xia, and L. F. Bosart, 2019: An Objective Classification and Analysis of Upper-Level Coupling to the Great Plains Low-Level Jet over the Twentieth Century. *Journal of Climate*, **32 (21)**, 7127–7152, https://doi.org/10.1175/JCLI-D-18-0891.1, URL http://journals.ametsoc.org/doi/10.1175/JCLI-D-18-0891.1.

Chan, S. C., E. J. Kendon, H. J. Fowler, A. Kahraman, J. Crook, N. Ban, and A. F. Prein, 2023: Large-scale dynamics moderate impact-relevant changes to organised convective storms. *Communications Earth & Environment*, **4 (1)**, 8, https://doi.org/10.1038/s43247-022-00669-2, URL https://www.nature.com/articles/s43247-022-00669-2.

Chang, E. K. M., Y. Guo, and X. Xia, 2012: CMIP5 multimodel ensemble projection of storm track change under global warming. *Journal of Geophysical Research: Atmospheres*, **117 (D23)**, 2012JD018 578, https://doi.org/10.1029/2012JD018578, URL https://agupubs.onlinelibrary.wiley.com/doi/10.1029/2012JD018578.

Chasteen, M. B., and S. E. Koch, 2022: Multiscale Aspects of the 26–27 April 2011 Tornado Outbreak. Part II: Environmental Modifications and Upscale Feedbacks Arising from Latent Processes. *Monthly Weather Review*, **150 (2)**, 337–368, https://doi.org/10.1175/MWR-D-21-0014.1, URL https://journals.ametsoc.org/view/journals/mwre/150/2/MWR-D-21-0014.1.xml.

Chen, D., A. Dai, and A. Hall, 2021: The Convective-To-Total Precipitation Ratio and the "Drizzling" Bias in Climate Models. *Journal of Geophysical Research: Atmospheres*, **126 (16)**, https://doi.org/10.1029/2020JD034198, URL https://onlinelibrary.wiley.com/doi/10.1029/2020JD034198.

Chen, G., J. Lu, D. A. Burrows, and L. R. Leung, 2015: Local finite-amplitude wave activity as an objective diagnostic of midlatitude extreme weather. *Geophysical Research Letters*, **42 (24)**, https://doi.org/10.1002/2015GL066959, URL https://agupubs.onlinelibrary.wiley.com/doi/10.1002/2015GL066959.

Chen, J., A. Dai, Y. Zhang, and K. L. Rasmussen, 2020: Changes in Convective Available Potential Energy and Convective Inhibition under Global Warming. *Journal of Climate*, **33 (6)**,

Accepted for publication in *Journal of Climate*. DOI 10.1175/JCLI-D-24-0251.1.

2025–2050, https://doi.org/10.1175/JCLI-D-19-0461.1, URL http://journals.ametsoc.org/doi/10.1175/JCLI-D-19-0461.1.

Coniglio, M. C., J. Y. Hwang, and D. J. Stensrud, 2010: Environmental Factors in the Upscale Growth and Longevity of MCSs Derived from Rapid Update Cycle Analyses. *Monthly Weather Review*, **138 (9)**, 3514–3539, https://doi.org/10.1175/2010MWR3233.1, URL http://journals.ametsoc.org/doi/10.1175/2010MWR3233.1.

Cotton, W., G. Alexander, R. Hertenstein, R. Walko, R. McAnelly, and M. Nicholls, 1995: Cloud venting — A review and some new global annual estimates. *Earth-Science Reviews*, **39 (3-4)**, 169–206, https://doi.org/10.1016/0012-8252(95)00007-0, URL https://linkinghub.elsevier.com/retrieve/pii/0012825295000070.

Dai, A., R. M. Rasmussen, K. Ikeda, and C. Liu, 2020: A new approach to construct representative future forcing data for dynamic downscaling. *Climate Dynamics*, **55 (1-2)**, 315–323, https://doi.org/10.1007/s00382-017-3708-8, URL http://link.springer.com/10.1007/s00382-017-3708-8.

Demaria, E. M. C., P. Hazenberg, R. L. Scott, M. B. Meles, M. Nichols, and D. Goodrich, 2019: Intensification of the North American Monsoon Rainfall as Observed From a Long-Term High-Density Gauge Network. *Geophysical Research Letters*, **46 (12)**, 6839–6847, https://doi.org/10.1029/2019GL082461, URL https://onlinelibrary.wiley.com/doi/abs/10.1029/2019GL082461.

Dougherty, E. M., A. F. Prein, E. D. Gutmann, and A. J. Newman, 2023: Future Simulated Changes in Central U.S. Mesoscale Convective System Rainfall Caused by Changes in Convective and Stratiform Structure. *Journal of Geophysical Research: Atmospheres*, **128 (4)**, e2022JD037 537, https://doi.org/10.1029/2022JD037537, URL https://agupubs.onlinelibrary.wiley.com/doi/10.1029/2022JD037537.

Feng, Z., R. A. Houze, L. R. Leung, F. Song, J. C. Hardin, J. Wang, W. I. Gustafson, and C. R. Homeyer, 2019: Spatiotemporal Characteristics and Large-Scale Environments of Mesoscale Convective Systems East of the Rocky Mountains. *Journal of Climate*, **32 (21)**, 7303–7328, https://doi.org/10.1175/JCLI-D-19-0137.1, URL https://journals.ametsoc.org/doi/10.1175/JCLI-D-19-0137.1.

Accepted for publication in *Journal of Climate*. DOI 10.1175/JCLI-D-24-0251.1.

Feng, Z., L. R. Leung, S. Hagos, R. A. Houze, C. D. Burleyson, and K. Balaguru, 2016: More frequent intense and long-lived storms dominate the springtime trend in central US rainfall. *Nature Communications*, **7 (1)**, 13 429, https://doi.org/10.1038/ncomms13429, URL https://www.nature.com/articles/ncomms13429.

Feng, Z., F. Song, K. Sakaguchi, and L. R. Leung, 2021a: Evaluation of Mesoscale Convective Systems in Climate Simulations: Methodological Development and Results from MPAS-CAM over the United States. *Journal of Climate*, **34 (7)**, 2611–2633, https://doi.org/10.1175/JCLI-D-20-0136.1, URL https://journals.ametsoc.org/view/journals/clim/34/7/JCLI-D-20-0136.1.xml.

Feng, Z., and Coauthors, 2021b: A Global High-Resolution Mesoscale Convective System Database Using Satellite-Derived Cloud Tops, Surface Precipitation, and Tracking. *Journal of Geophysical Research: Atmospheres*, **126 (8)**, e2020JD034 202, https://doi.org/10.1029/2020JD034202, URL https://agupubs.onlinelibrary.wiley.com/doi/10.1029/2020JD034202.

Ferguson, C. R., 2022: Changes in Great Plains Low-Level Jet Structure and Associated Precipitation Over the 20th Century. *Journal of Geophysical Research: Atmospheres*, **127 (3)**, e2021JD035 859, https://doi.org/10.1029/2021JD035859, URL https://agupubs.onlinelibrary.wiley.com/doi/10.1029/2021JD035859.

Ferreira, R. N., and T. M. Rickenbach, 2021: Mechanisms for Springtime Onset of Isolated Precipitation across the Southeastern United States. *Atmosphere*, **12 (2)**, 213, https://doi.org/10.3390/atmos12020213, URL https://www.mdpi.com/2073-4433/12/2/213.

Fischer, E. M., and R. Knutti, 2016: Observed heavy precipitation increase confirms theory and early models. *Nature Climate Change*, **6 (11)**, 986–991, https://doi.org/10.1038/nclimate3110, URL https://www.nature.com/articles/nclimate3110.

Fitzpatrick, R. G. J., and Coauthors, 2020: What Drives the Intensification of Mesoscale Convective Systems over the West African Sahel under Climate Change? *Journal of Climate*, **33 (8)**, 3151–3172, https://doi.org/10.1175/JCLI-D-19-0380.1, URL https://journals.ametsoc.org/doi/10.1175/JCLI-D-19-0380.1.

Accepted for publication in *Journal of Climate*. DOI 10.1175/JCLI-D-24-0251.1.

Fritzen, R., V. Lang, and V. A. Gensini, 2021: Trends and variability of north american cool-season extratropical cyclones: 1979–2019. *Journal of Applied Meteorology and Climatology*, https://doi.org/10.1175/jamc-d-20-0276.1, URL http://dx.doi.org/10.1175/JAMC-D-20-0276.1.

Fu, D., P. Chang, C. M. Patricola, R. Saravanan, X. Liu, and H. E. Beck, 2021: Central American mountains inhibit eastern North Pacific seasonal tropical cyclone activity. *Nature Communications*, **12 (1)**, 4422, https://doi.org/10.1038/s41467-021-24657-w, URL http://www.nature.com/articles/s41467-021-24657-w.

Gao, Y., L. R. Leung, C. Zhao, and S. Hagos, 2017: Sensitivity of U.S. summer precipitation to model resolution and convective parameterizations across gray zone resolutions: Sensitivity Across Gray Zone Resolutions. *Journal of Geophysical Research: Atmospheres*, **122 (5)**, 2714–2733, https://doi.org/10.1002/2016JD025896, URL http://doi.wiley.com/10.1002/2016JD025896.

Gensini, V. A., A. M. Haberlie, and W. S. Ashley, 2023: Convection-permitting simulations of historical and possible future climate over the contiguous United States. *Climate Dynamics*, https://doi.org/10.1007/s00382-022-06306-0, URL https://link.springer.com/10.1007/s00382-022-06306-0.

Gensini, V. A., and T. L. Mote, 2014: Estimations of Hazardous Convective Weather in the United States Using Dynamical Downscaling. *Journal of Climate*, **27 (17)**, 6581–6589, https://doi.org/10.1175/JCLI-D-13-00777.1, URL http://journals.ametsoc.org/doi/10.1175/JCLI-D-13-00777.1.

Giorgi, F., and W. J. Gutowski, 2015: Regional Dynamical Downscaling and the CORDEX Initiative. *Annual Review of Environment and Resources*, **40 (1)**, 467–490, https://doi.org/10.1146/annurev-environ-102014-021217, URL https://www.annualreviews.org/doi/10.1146/annurev-environ-102014-021217.

Haberlie, A. M., and W. S. Ashley, 2019a: Climatological representation of mesoscale convective systems in a dynamically downscaled climate simulation. *International Journal of Climatology*, **39 (2)**, 1144–1153, https://doi.org/10.1002/joc.5880, URL https://onlinelibrary.wiley.com/doi/10.1002/joc.5880.

Accepted for publication in *Journal of Climate*. DOI 10.1175/JCLI-D-24-0251.1.

Haberlie, A. M., and W. S. Ashley, 2019b: A Radar-Based Climatology of Mesoscale Convective Systems in the United States. *Journal of Climate*, **32 (5)**, 1591–1606, https://doi.org/10.1175/JCLI-D-18-0559.1, URL http://journals.ametsoc.org/doi/10.1175/JCLI-D-18-0559.1.

Haberlie, A. M., W. S. Ashley, C. M. Battisto, and V. A. Gensini, 2022: Thunderstorm Activity Under Intermediate and Extreme Climate Change Scenarios. *Geophysical Research Letters*, **49 (14)**, e2022GL098 779, https://doi.org/10.1029/2022GL098779, URL https://agupubs.onlinelibrary.wiley.com/doi/10.1029/2022GL098779.

Haberlie, A. M., W. S. Ashley, V. A. Gensini, and A. C. Michaelis, 2023: The ratio of mesoscale convective system precipitation to total precipitation increases in future climate change scenarios. *npj Climate and Atmospheric Science*, **6 (1)**, 150, https://doi.org/10.1038/s41612-023-00481-5, URL https://www.nature.com/articles/s41612-023-00481-5.

Haberlie, A. M., B. Wallace, W. S. Ashley, A. C. Michaelis, and V. A. Gensini, 2024: Mesoscale convective system activity in the united states under intermediate and extreme climate change scenarios. *Climatic Change*, under review.

Hardwick Jones, R., S. Westra, and A. Sharma, 2010: Observed relationships between extreme sub-daily precipitation, surface temperature, and relative humidity: RELATIONSHIP BETWEEN PRECIP, TEMP, AND RH. *Geophysical Research Letters*, **37 (22)**, n/a–n/a, https://doi.org/10.1029/2010GL045081, URL http://doi.wiley.com/10.1029/2010GL045081.

Held, I. M., and B. J. Soden, 2006: Robust Responses of the Hydrological Cycle to Global Warming. *Journal of Climate*, **19 (21)**, 5686–5699, https://doi.org/10.1175/JCLI3990.1, URL http://journals.ametsoc.org/doi/10.1175/JCLI3990.1.

Hoogewind, K. A., M. E. Baldwin, and R. J. Trapp, 2017: The Impact of Climate Change on Hazardous Convective Weather in the United States: Insight from High-Resolution Dynamical Downscaling. *Journal of Climate*, **30 (24)**, 10 081–10 100, https://doi.org/10.1175/JCLI-D-16-0885.1, URL https://journals.ametsoc.org/doi/10.1175/JCLI-D-16-0885.1.

Houze, R. A., 2004: Mesoscale convective systems. *Reviews of Geophysics*, **42 (4)**, 2004RG000 150, https://doi.org/10.1029/2004RG000150, URL https://agupubs.onlinelibrary.wiley.com/doi/10.1029/2004RG000150.

Accepted for publication in *Journal of Climate*. DOI 10.1175/JCLI-D-24-0251.1.

Hu, H., L. R. Leung, and Z. Feng, 2020: Observed Warm-Season Characteristics of MCS and Non-MCS Rainfall and Their Recent Changes in the Central United States. *Geophysical Research Letters*, **47 (6)**, e2019GL086 783, https://doi.org/10.1029/2019GL086783, URL https://agupubs.onlinelibrary.wiley.com/doi/10.1029/2019GL086783.

Hu, H., L. R. Leung, and Z. Feng, 2021: Early warm-season mesoscale convective systems dominate soil moisture–precipitation feedback for summer rainfall in central United States. *Proceedings of the National Academy of Sciences*, **118 (43)**, e2105260 118, https://doi.org/10.1073/pnas.2105260118, URL https://pnas.org/doi/full/10.1073/pnas.2105260118.

Huang, C. S. Y., and N. Nakamura, 2016: Local Finite-Amplitude Wave Activity as a Diagnostic of Anomalous Weather Events. *Journal of the Atmospheric Sciences*, **73 (1)**, 211–229, https://doi.org/10.1175/JAS-D-15-0194.1, URL https://journals.ametsoc.org/doi/10.1175/JAS-D-15-0194.1.

Hurrell, J. W., M. M. Holland, P. R. Gent, S. Ghan, J. E. Kay, and P. J. Kushner, 2013: THE COMMUNITY EARTH SYSTEM MODEL.

Jankov, I., and W. A. Gallus, 2004: Mcs rainfall forecast accuracy as a function of large-scale forcing. *Weather and Forecasting*, **19 (2)**, 428–439, https://doi.org/10.1175/1520-0434(2004)019⟨0428:mrfaaa⟩2.0.co;2, URL http://dx.doi.org/10.1175/1520-0434(2004)019⟨0428:MRFAAA⟩2.0.CO;2.

Kharin, V. V., F. W. Zwiers, X. Zhang, and M. Wehner, 2013: Changes in temperature and precipitation extremes in the CMIP5 ensemble. *Climatic Change*, **119 (2)**, 345–357, https://doi.org/10.1007/s10584-013-0705-8, URL http://link.springer.com/10.1007/s10584-013-0705-8.

Koch, S. E., B. Ferrier, M. Stolinga, E. Szoke, S. J. Weiss, and J. S. Kain, 2005: The use of simulated radar reflectivity fields in the diagnosis of mesoscale phenomena from high-resolution wrf model forecasts. *Preprints, 12th Conference on Mesoscale Processes*, Albuquerque, NM, American Meteorlogical Society, J4J.7.

Laing, A. G., and J. M. Fritsch, 2000: The Large-Scale Environments of the Global Populations of Mesoscale Convective Complexes. *Monthly Weather Review*, **128 (8)**, 2756–2776,

Accepted for publication in *Journal of Climate*. DOI 10.1175/JCLI-D-24-0251.1.

https://doi.org/10.1175/1520-0493(2000)128⟨2756:TLSEOT⟩2.0.CO;2, URL http://journals.ametsoc.org/doi/10.1175/1520-0493(2000)128⟨2756:TLSEOT⟩2.0.CO;2.

Lasher-Trapp, S., S. A. Orendorf, and R. J. Trapp, 2023: Investigating a Derecho in a Future Warmer Climate. *Bulletin of the American Meteorological Society*, **104 (10)**, E1831–E1852, https://doi.org/10.1175/BAMS-D-22-0173.1, URL https://journals.ametsoc.org/view/journals/bams/104/10/BAMS-D-22-0173.1.xml.

Leutwyler, D., D. Lüthi, N. Ban, O. Fuhrer, and C. Schär, 2017: Evaluation of the convection-resolving climate modeling approach on continental scales: CONVECTION-RESOLVING CONTINENTAL-SCALE SIMULATION. *Journal of Geophysical Research: Atmospheres*, **122 (10)**, 5237–5258, https://doi.org/10.1002/2016JD026013, URL http://doi.wiley.com/10.1002/2016JD026013.

Li, L., W. Li, and Y. Kushnir, 2012: Variation of the North Atlantic subtropical high western ridge and its implication to Southeastern US summer precipitation. *Climate Dynamics*, **39 (6)**, 1401–1412, https://doi.org/10.1007/s00382-011-1214-y, URL http://link.springer.com/10.1007/s00382-011-1214-y.

Li, W., L. Li, R. Fu, Y. Deng, and H. Wang, 2011: Changes to the North Atlantic Subtropical High and Its Role in the Intensification of Summer Rainfall Variability in the Southeastern United States. *Journal of Climate*, **24 (5)**, 1499–1506, https://doi.org/10.1175/2010JCLI3829.1, URL http://journals.ametsoc.org/doi/10.1175/2010JCLI3829.1.

Liu, C., and Coauthors, 2017: Continental-scale convection-permitting modeling of the current and future climate of North America. *Climate Dynamics*, **49 (1-2)**, 71–95, https://doi.org/10.1007/s00382-016-3327-9, URL http://link.springer.com/10.1007/s00382-016-3327-9.

Martineau, P., G. Chen, and D. A. Burrows, 2017: Wave Events: Climatology, Trends, and Relationship to Northern Hemisphere Winter Blocking and Weather Extremes. *Journal of Climate*, **30 (15)**, 5675–5697, https://doi.org/10.1175/JCLI-D-16-0692.1, URL https://journals.ametsoc.org/doi/10.1175/JCLI-D-16-0692.1.

McCabe, G. J., M. P. Clark, and M. C. Serreze, 2001: Trends in Northern Hemisphere Surface Cyclone Frequency and Intensity. *Journal of Climate*, **14 (12)**, 2763–2768, https://doi.org/

Accepted for publication in *Journal of Climate*. DOI 10.1175/JCLI-D-24-0251.1.

10.1175/1520-0442(2001)014⟨2763:TINHSC⟩2.0.CO;2, URL http://journals.ametsoc.org/doi/10.1175/1520-0442(2001)014⟨2763:TINHSC⟩2.0.CO;2.

Miguez-Macho, G., G. L. Stenchikov, and A. Robock, 2004: Spectral nudging to eliminate the effects of domain position and geometry in regional climate model simulations: SPECTRAL NUDGING IN REGIONAL MODELS. *Journal of Geophysical Research: Atmospheres*, **109 (D13)**, n/a–n/a, https://doi.org/10.1029/2003JD004495, URL http://doi.wiley.com/10.1029/2003JD004495.

Monaghan, A. J., D. F. Steinhoff, C. L. Bruyere, and D. Yates, 2014: Ncar cesm global bias-corrected cmip5 output to support wrf/mpas research. Research Data Archive at the National Center for Atmospheric Research, Computational and Information Systems Laboratory, Boulder CO, URL https://doi.org/10.5065/D6DJ5CN4.

Moss, R. H., and Coauthors, 2010: The next generation of scenarios for climate change research and assessment. *Nature*, **463 (7282)**, 747–756, https://doi.org/10.1038/nature08823, URL http://www.nature.com/articles/nature08823.

Na, Y., Q. Fu, L. R. Leung, C. Kodama, and R. Lu, 2022: Mesoscale Convective Systems Simulated by a High-Resolution Global Nonhydrostatic Model Over the United States and China. *Journal of Geophysical Research: Atmospheres*, **127 (7)**, e2021JD035 916, https://doi.org/10.1029/2021JD035916, URL https://agupubs.onlinelibrary.wiley.com/doi/10.1029/2021JD035916.

Nakanishi, M., and H. Niino, 2006: An improved mellor–yamada level-3 model: Its numerical stability and application to a regional prediction of advection fog. *Boundary-Layer Meteorology*, **119 (2)**, 397–407, https://doi.org/10.1007/s10546-005-9030-8, URL https://doi.org/10.1007/s10546-005-9030-8.

Nesbitt, S. W., R. Cifelli, and S. A. Rutledge, 2006: Storm Morphology and Rainfall Characteristics of TRMM Precipitation Features. *Monthly Weather Review*, **134 (10)**, 2702–2721, https://doi.org/10.1175/MWR3200.1, URL http://journals.ametsoc.org/doi/10.1175/MWR3200.1.

Nieto Ferreira, R., and T. M. Rickenbach, 2020: Effects of the North Atlantic Subtropical High on summertime precipitation organization in the southeast United States. *Interna-*

Accepted for publication in *Journal of Climate*. DOI 10.1175/JCLI-D-24-0251.1.

tional Journal of Climatology, **40 (14)**, 5987–6001, https://doi.org/10.1002/joc.6561, URL https://rmets.onlinelibrary.wiley.com/doi/10.1002/joc.6561.

O'Brien, T. A., W. D. Collins, K. Kashinath, O. Rübel, S. Byna, J. Gu, H. Krishnan, and P. A. Ullrich, 2016: Resolution dependence of precipitation statistical fidelity in hindcast simulations: ILIAD SIMULATIONS OF PRECIPITATION. *Journal of Advances in Modeling Earth Systems*, **8 (2)**, 976–990, https://doi.org/10.1002/2016MS000671, URL http://doi.wiley.com/10.1002/2016MS000671.

Pendergrass, A. G., 2020: The Global-Mean Precipitation Response to CO_2 -Induced Warming in CMIP6 Models. *Geophysical Research Letters*, **47 (17)**, https://doi.org/10.1029/2020GL089964, URL https://onlinelibrary.wiley.com/doi/10.1029/2020GL089964.

Peters, J. M., and R. S. Schumacher, 2014: Objective Categorization of Heavy-Rain-Producing MCS Synoptic Types by Rotated Principal Component Analysis. *Monthly Weather Review*, **142 (5)**, 1716–1737, https://doi.org/10.1175/MWR-D-13-00295.1, URL http://journals.ametsoc.org/doi/10.1175/MWR-D-13-00295.1.

Pfahl, S., P. A. O'Gorman, and E. M. Fischer, 2017: Understanding the regional pattern of projected future changes in extreme precipitation. *Nature Climate Change*, **7 (6)**, 423–427, https://doi.org/10.1038/nclimate3287, URL http://www.nature.com/articles/nclimate3287.

Pokharel, B., S.-Y. S. Wang, J. Meyer, R. Gillies, and Y.-H. Lin, 2019: Climate of the weakly-forced yet high-impact convective storms throughout the Ohio River Valley and Mid-Atlantic United States. *Climate Dynamics*, **52 (9-10)**, 5709–5721, https://doi.org/10.1007/s00382-018-4472-0, URL http://link.springer.com/10.1007/s00382-018-4472-0.

Prein, A. F., C. Liu, K. Ikeda, R. Bullock, R. M. Rasmussen, G. J. Holland, and M. Clark, 2020: Simulating North American mesoscale convective systems with a convection-permitting climate model. *Climate Dynamics*, **55 (1-2)**, 95–110, https://doi.org/10.1007/s00382-017-3993-2, URL http://link.springer.com/10.1007/s00382-017-3993-2.

Prein, A. F., C. Liu, K. Ikeda, S. B. Trier, R. M. Rasmussen, G. J. Holland, and M. P. Clark, 2017a: Increased rainfall volume from future convective storms in the US. *Nature Climate*

Accepted for publication in *Journal of Climate*. DOI 10.1175/JCLI-D-24-0251.1.

Change, **7 (12)**, 880–884, https://doi.org/10.1038/s41558-017-0007-7, URL http://www.nature.com/articles/s41558-017-0007-7.

Prein, A. F., R. M. Rasmussen, K. Ikeda, C. Liu, M. P. Clark, and G. J. Holland, 2017b: The future intensification of hourly precipitation extremes. *Nature Climate Change*, **7 (1)**, 48–52, https://doi.org/10.1038/nclimate3168, URL http://www.nature.com/articles/nclimate3168.

Prein, A. F., R. M. Rasmussen, D. Wang, and S. E. Giangrande, 2021: Sensitivity of organized convective storms to model grid spacing in current and future climates. *Philosophical Transactions of the Royal Society A: Mathematical, Physical and Engineering Sciences*, **379 (2195)**, 20190 546, https://doi.org/10.1098/rsta.2019.0546, URL https://royalsocietypublishing.org/doi/10.1098/rsta.2019.0546.

Prein, A. F., and Coauthors, 2015: A review on regional convection-permitting climate modeling: Demonstrations, prospects, and challenges. *Reviews of Geophysics*, **53 (2)**, 323–361, https://doi.org/10.1002/2014RG000475, URL https://onlinelibrary.wiley.com/doi/10.1002/2014RG000475.

Rasmussen, K. L., A. F. Prein, R. M. Rasmussen, K. Ikeda, and C. Liu, 2020: Changes in the convective population and thermodynamic environments in convection-permitting regional climate simulations over the United States. *Climate Dynamics*, **55 (1-2)**, 383–408, https://doi.org/10.1007/s00382-017-4000-7, URL http://link.springer.com/10.1007/s00382-017-4000-7.

Rasmussen, R., and Coauthors, 2011: High-Resolution Coupled Climate Runoff Simulations of Seasonal Snowfall over Colorado: A Process Study of Current and Warmer Climate. *Journal of Climate*, **24 (12)**, 3015–3048, https://doi.org/10.1175/2010JCLI3985.1, URL http://journals.ametsoc.org/doi/10.1175/2010JCLI3985.1.

Rauscher, S. A., T. A. O'Brien, C. Piani, E. Coppola, F. Giorgi, W. D. Collins, and P. M. Lawston, 2016: A multimodel intercomparison of resolution effects on precipitation: simulations and theory. *Climate Dynamics*, **47 (7-8)**, 2205–2218, https://doi.org/10.1007/s00382-015-2959-5, URL http://link.springer.com/10.1007/s00382-015-2959-5.

Schemm, S., S. Rüdisühli, and M. Sprenger, 2020: The life cycle of upper-level troughs and ridges: a novel detection method, climatologies and Lagrangian characteristics. *Weather and*

Accepted for publication in *Journal of Climate*. DOI 10.1175/JCLI-D-24-0251.1.

Climate Dynamics, **1 (2)**, 459–479, https://doi.org/10.5194/wcd-1-459-2020, URL https://wcd.copernicus.org/articles/1/459/2020/.

Schumacher, R. S., and R. H. Johnson, 2005: Organization and Environmental Properties of Extreme-Rain-Producing Mesoscale Convective Systems. *Monthly Weather Review*, **133 (4)**, 961–976, https://doi.org/10.1175/MWR2899.1, URL https://journals.ametsoc.org/doi/10.1175/MWR2899.1.

Schumacher, R. S., and R. H. Johnson, 2006: Characteristics of U.S. Extreme Rain Events during 1999–2003. *Weather and Forecasting*, **21 (1)**, 69–85, https://doi.org/10.1175/WAF900.1, URL https://journals.ametsoc.org/doi/10.1175/WAF900.1.

Schumacher, R. S., and K. L. Rasmussen, 2020: The formation, character and changing nature of mesoscale convective systems. *Nature Reviews Earth & Environment*, **1 (6)**, 300–314, https://doi.org/10.1038/s43017-020-0057-7, URL https://www.nature.com/articles/s43017-020-0057-7.

Schär, C., C. Frei, D. Lüthi, and H. C. Davies, 1996: Surrogate climate-change scenarios for regional climate models. *Geophysical Research Letters*, **23 (6)**, 669–672, https://doi.org/10.1029/96GL00265, URL http://doi.wiley.com/10.1029/96GL00265.

Seager, R., N. Naik, and G. A. Vecchi, 2010: Thermodynamic and Dynamic Mechanisms for Large-Scale Changes in the Hydrological Cycle in Response to Global Warming*. *Journal of Climate*, **23 (17)**, 4651–4668, https://doi.org/10.1175/2010JCLI3655.1, URL http://journals.ametsoc.org/doi/10.1175/2010JCLI3655.1.

Skamarock, W. C., and Coauthors, 2019: A description of the advanced research wrf model version 4. https://doi.org/10.5065/1DFH-6P97, URL https://opensky.ucar.edu/islandora/object/opensky:2898.

Song, F., Z. Feng, L. R. Leung, R. A. Houze Jr., J. Wang, J. Hardin, and C. R. Homeyer, 2019: Contrasting Spring and Summer Large-Scale Environments Associated with Mesoscale Convective Systems over the U.S. Great Plains. *Journal of Climate*, **32 (20)**, 6749–6767, https://doi.org/10.1175/JCLI-D-18-0839.1, URL http://journals.ametsoc.org/doi/10.1175/JCLI-D-18-0839.1.

Accepted for publication in *Journal of Climate*. DOI 10.1175/JCLI-D-24-0251.1.

Song, F., Z. Feng, L. R. Leung, B. Pokharel, S. S. Wang, X. Chen, K. Sakaguchi, and C. Wang, 2021: Crucial Roles of Eastward Propagating Environments in the Summer MCS Initiation Over the U.S. Great Plains. *Journal of Geophysical Research: Atmospheres*, **126 (16)**, e2021JD034 991, https://doi.org/10.1029/2021JD034991, URL https://agupubs.onlinelibrary.wiley.com/doi/10.1029/2021JD034991.

Song, F., L. R. Leung, Z. Feng, X. Chen, and Q. Yang, 2022: Observed and Projected Changes of Large-Scale Environments Conducive to Spring MCS Initiation Over the US Great Plains. *Geophysical Research Letters*, **49 (15)**, e2022GL098 799, https://doi.org/10.1029/2022GL098799, URL https://agupubs.onlinelibrary.wiley.com/doi/10.1029/2022GL098799.

Song, F., L. R. Leung, J. Lu, and L. Dong, 2018a: Future Changes in Seasonality of the North Pacific and North Atlantic Subtropical Highs. *Geophysical Research Letters*, **45 (21)**, https://doi.org/10.1029/2018GL079940, URL https://agupubs.onlinelibrary.wiley.com/doi/10.1029/2018GL079940.

Song, F., L. R. Leung, J. Lu, and L. Dong, 2018b: Seasonally dependent responses of subtropical highs and tropical rainfall to anthropogenic warming. *Nature Climate Change*, **8 (9)**, 787–792, https://doi.org/10.1038/s41558-018-0244-4, URL http://www.nature.com/articles/s41558-018-0244-4.

Taylor, C. M., and Coauthors, 2017: Frequency of extreme Sahelian storms tripled since 1982 in satellite observations. *Nature*, **544 (7651)**, 475–478, https://doi.org/10.1038/nature22069, URL https://www.nature.com/articles/nature22069.

Trenberth, K. E., A. Dai, R. M. Rasmussen, and D. B. Parsons, 2003: The Changing Character of Precipitation. *Bulletin of the American Meteorological Society*, **84 (9)**, 1205–1218, https://doi.org/10.1175/BAMS-84-9-1205, URL https://journals.ametsoc.org/doi/10.1175/BAMS-84-9-1205.

Trenberth, K. E., and D. P. Stepaniak, 2003: Covariability of Components of Poleward Atmospheric Energy Transports on Seasonal and Interannual Timescales. *Journal of Climate*, **16 (22)**, 3691–3705, https://doi.org/10.1175/1520-0442(2003)016⟨3691:COCOPA⟩2.0.CO;2, URL http://journals.ametsoc.org/doi/10.1175/1520-0442(2003)016⟨3691:COCOPA⟩2.0.CO;2.

Accepted for publication in *Journal of Climate*. DOI 10.1175/JCLI-D-24-0251.1.

Wallace, B., and J. R. Minder, 2024: The sensitivity of the North American Monsoon to Gulf of California Sea surface temperatures. *Climate Dynamics*, https://doi.org/10.1007/s00382-023-07057-2, URL https://link.springer.com/10.1007/s00382-023-07057-2.

Wallace, B. C., 2024: $bc-wallace/mcs_paper_2024 : v0.2$. Zenodo, URL https://zenodo.org/doi/10.5281/zenodo.11111270, https://doi.org/10.5281/ZENODO.11111270.

Wallace, B. C., A. M. Haberlie, W. S. Ashley, V. A. Gensini, and A. C. Michaelis, 2023: Decomposing the Precipitation Response to Climate Change in Convection Allowing Simulations Over the Conterminous United States. *Earth and Space Science*, **10 (12)**, e2023EA003 094, https://doi.org/10.1029/2023EA003094, URL https://agupubs.onlinelibrary.wiley.com/doi/10.1029/2023EA003094.

Wu, Y., M. Ting, R. Seager, H.-P. Huang, and M. A. Cane, 2011: Changes in storm tracks and energy transports in a warmer climate simulated by the GFDL CM2.1 model. *Climate Dynamics*, **37 (1-2)**, 53–72, https://doi.org/10.1007/s00382-010-0776-4, URL http://link.springer.com/10.1007/s00382-010-0776-4.

Yang, Q., R. A. Houze, L. R. Leung, and Z. Feng, 2017: Environments of Long-Lived Mesoscale Convective Systems Over the Central United States in Convection Permitting Climate Simulations. *Journal of Geophysical Research: Atmospheres*, **122 (24)**, https://doi.org/10.1002/2017JD027033, URL https://onlinelibrary.wiley.com/doi/10.1002/2017JD027033.

Yin, J. H., 2005: A consistent poleward shift of the storm tracks in simulations of 21st century climate. *Geophysical Research Letters*, **32 (18)**, 2005GL023 684, https://doi.org/10.1029/2005GL023684, URL https://agupubs.onlinelibrary.wiley.com/doi/10.1029/2005GL023684.

Zhang, H., Y. Gao, J. Xu, Y. Xu, and Y. Jiang, 2019: Decomposition of Future Moisture Flux Changes over the Tibetan Plateau Projected by Global and Regional Climate Models. *Journal of Climate*, **32 (20)**, 7037–7053, https://doi.org/10.1175/JCLI-D-19-0200.1, URL http://journals.ametsoc.org/doi/10.1175/JCLI-D-19-0200.1.

Zhou, W., L. R. Leung, F. Song, and J. Lu, 2021: Future Changes in the Great Plains Low-Level Jet Governed by Seasonally Dependent Pattern Changes in the North Atlantic Subtropical High. *Geo-*

Accepted for publication in *Journal of Climate*. DOI 10.1175/JCLI-D-24-0251.1.

physical Research Letters, **48 (4)**, e2020GL090 356, https://doi.org/10.1029/2020GL090356, URL https://agupubs.onlinelibrary.wiley.com/doi/10.1029/2020GL090356.

Zishka, K. M., and P. J. Smith, 1980: The climatology of cyclones and anticyclones over north america and surrounding ocean environs for january and july, 1950–77. *Monthly Weather Review*, **108 (4)**, 387–401, https://doi.org/10.1175/1520-0493(1980)108⟨0387:tcocaa⟩2.0.co;2, URL http://dx.doi.org/10.1175/1520-0493(1980)108⟨0387:TCOCAA⟩2.0.CO;2.

Accepted for publication in *Journal of Climate*. DOI 10.1175/JCLI-D-24-0251.1.